




Compression-only behavior: Effect of prestress and shell rheology on bifurcation diagrams and parametric stability of coated microbubbles in an unbounded flow

Nikos Pelekasis ,* Maria Vlachomitrou , and Alkmini Lytra 

Department of Mechanical Engineering, University of Thessaly, Leoforos Athinon, Pedion Areos 38334 Volos, Greece



(Received 6 April 2022; accepted 21 October 2022; published 15 November 2022)

Lipid-shelled microbubbles exhibit a strain-softening behavior and thus are characterized by preferential excursion from equilibrium during expansion at insonation. However, experimental studies have reported a counterintuitive behavior, identified as the compression-only behavior, where they pulsate mainly in the compression phase. We construct bifurcation diagrams of lipid and polymer-shelled microbubbles indicating the existence of a parameter range for which buckled shapes that are characterized by significantly smaller volume and lower total energy level, in comparison with the spherically symmetric state, are expected to spontaneously arise. The timescale for such a transition depends on the amplitude and frequency of the initial disturbance but more importantly on shell rheology in terms of the bending vs area dilatation modulus and shear vs dilatational viscosity. We show by performing stability analysis and constructing phase diagrams of coated microbubbles that an initially prestressed shell facilitates the onset of buckling at relatively small sound amplitudes. Moreover, low values of the shell bending modulus and shear viscosity in comparison with the area dilatation modulus and dilatational viscosity, respectively, facilitate the onset of shape modes that characterize bifurcating branches leading to deformed shapes with significant volume compression at relatively low sound amplitudes. By performing dynamic simulations for lipid-shelled microbubbles, we capture the onset of compression-only effect during which the shell tends to oscillate around compressed buckled shapes when subject to an acoustic disturbance. When phase diagrams of polymeric shells are examined the amplitude threshold for dynamic buckling to occur typically arrives before the onset of parametric shape mode excitation. Therefore the shell cohesion is compromised before it achieves a steady pulsation around a compressed shape, and this is verified by our simulations.

DOI: [10.1103/PhysRevFluids.7.113601](https://doi.org/10.1103/PhysRevFluids.7.113601)

I. INTRODUCTION

Contrast agents are gas-filled encapsulated microbubbles that are used in novel biomedical applications involving ultrasound such as targeted drug delivery [1] and medical imaging of vital organs [2]. Their coating is usually a lipid monolayer or a polymeric material with the former shells exhibiting a strain-softening behavior when subjected to acoustic disturbances [3–5]. This behavior is a result of the reduction in area density of the lipid monolayer shell with increasing interfacial area, which amounts to a preferential excursion from equilibrium during expansion [3,6] especially at large sound amplitudes. However, certain experimental studies [6,7] have revealed a counterintuitive behavior of lipid monolayer shells whereby they pulsate mainly in the compression phase of

*pel@uth.gr

their radial time series. The latter studies involved ultrafast imaging experiments with phospholipid microbubbles, i.e., SonoVue and BR-14, and studied their response to external frequencies in the range of 1, 1.8, and 4 MHz and acoustic amplitudes in the range between 50 and 200 kPa. In this fashion they reported that 40% of the bubbles showed a compression-only behavior for 1 MHz driving frequency and 50 kPa amplitude. They speculated that this behavior is triggered due to a small shrinkage of the bubbles that occurs after preparation of the sample, when a small amount of the interior gas diffuses into the liquid. An interesting aspect of this response type is that it has only been reported in experiments involving lipid-shelled contrast agents instead of polymeric shells, a fact that implies strong dependence on shell properties.

The theoretical aspect of this phenomenon has not yet been fully understood since the proper modeling of lipid-encapsulated bubbles is quite complex mainly due to inadequate information and difficulty to obtain reliable estimates of shell rheological parameters. The failure of preexisting shell models to capture the compression-only behavior observed in experiments has led researchers to introduce more sophisticated models that assume dependence of the rheological shell parameters on the bubble radius. In fact, there is still an open discussion regarding the mechanism of the compression-only behavior of lipid-shelled contrast agents. In particular, Marmottant *et al.* [7] introduced a model that allows for modification of the rheological parameters of the shell as the bubble oscillates. More specifically, they assumed a surface tension that depends highly on the surface concentration of phospholipid molecules. In this fashion when the bubble is highly compressed the shell is treated as a buckled solid phase and a zero-surface tension is assumed. As the bubble expands above a critical limit an elastic state is entered where the surface tension depends linearly on the area of the shell. In this state as the bubble expands the density of the molecules on the interface decreases and consequently the effective surface tension increases. An upper bound in the expansion radius is introduced above which a ruptured state is assumed, and any further expansion treats the bubble as a pure gas phase with the surface tension being equal to the one between water and air. In this context, the above researchers captured the compression-only behavior when they considered the initial radius of the bubble to be the critical limit below which a solid state is assumed for the shell. They attributed the initially compressed state of the bubble to the dissolution of a certain amount of gas in the surrounding liquid that happens either spontaneously or due to the repeated pulses imposed on the interface. This approach has been adopted in other studies as well [8,9]. However, it does not introduce a proper elastic model for the shell as an elastic material and assumes zero bending modulus to allow for buckling to take place at compression as indicated by experiments [10]. As a result, it compromises the robustness of the methodology for the acoustic characterization of coated microbubbles.

Using a different approach Doinikov *et al.* [11] introduced the shear-thinning behavior of the shell in order to include nonlinear effects in the variation of shell viscosity. In this fashion they were able to numerically capture compression-only behavior as reported by de Jong *et al.* [6] without however reliably recovering resonance frequencies of coated microbubbles based on acoustic measurements.

In the present study we treat the shell as a viscoelastic solid characterized by area dilatation and bending stiffness as well as shear and dilatational viscosity, in order to control the extent to which it deforms and buckles subject to acoustic or other disturbances. We also allow for a strain-softening shell behavior to account for the reduction of shell elasticity at expansion [3,9] and assume constant rheological shell properties that do not depend on the radius of the bubble. Furthermore, we adopt the assumption for an initially prestressed compressed shell due to gas leakage, originally proposed by Marmottant *et al.* [7], in order to capture shell buckling at a relatively small sound amplitude. We expect that shell viscosity plays a key role in the modeling of coated microbubbles, especially in the presence of surfactant monolayers [12], but the shear and dilatational components of membrane viscosity cannot be readily measured and consequently they are typically treated as equal [13]. However, in the present study we treat them as being different which allows for a more general and realistic description of shell rheology. Overall, we aim at capturing energy transfer from the breathing mode to shape modes associated with shell deformation and buckling, leading to the compression-only response pattern.

In this context, we carry out dynamic numerical simulations in an unbounded flow that demonstrate the onset of the compression-only behavior, and we define its mechanism based on the results of stability analysis. In particular, we investigate the static stability by performing a numerical study on the static response of coated microbubbles subject to an external overpressure, in the manner performed by Lytra and Pelekasis [14]. The latter approach resulted in bifurcation diagrams covering a wide parameter range that is relevant to acoustic characterization studies of lipid and polymeric shells. The goal is to identify different equilibrium configurations of the microbubble that may affect its response in the presence of acoustic disturbances and lead to oscillations around a reduced volume. In addition, the possibility for parametric instability to emerge is investigated, following Tsiglifis and Pelekasis [15] and introducing the effects of prestress and discrepancy in the shear and dilatational viscosities. We intend to capture a realistic route for the onset of shape modes that will grow and eventually lead to the buckled shapes predicted by the bifurcation diagrams of static analysis, thereby identifying a mechanism that may be responsible for the compression-only behavior of contrast agents coated with a lipid monolayer shell. An effort will also be made to account for discrepancies in the dynamic response of lipid and polymeric shells registered in the literature, in terms of the parametric stability of polymeric and lipid-shelled contrast agents. The lack of acoustic measurements that involve the former-type microbubbles exhibiting compression-only behavior will be interpreted in this fashion. Finally, the results obtained with the numerical simulations in an unbounded flow are presented and examined under the findings of static and parametric stability analysis.

This paper is organized as follows: the problem formulation is discussed in Sec. II, where the governing equations for the liquid flow are presented along with the ones describing the encapsulated bubble. Next, in Sec. III the stability analysis is presented: in Sec. III A we briefly discuss the method used for constructing the bifurcation diagrams, whereas in Sec. III B the details of parametric stability analysis are presented including the effects of prestress and different shear and dilatational shell viscosities. In Sec. IV the methodology employed for performing dynamic simulations is described. Subsequently, in Sec. V the results of parametric stability, static numerical analysis and numerical dynamic simulations are presented and cross-examined. Finally, in Sec. VI the main conclusions of the study are summarized.

II. PROBLEM FORMULATION

We consider an encapsulated microbubble of initial radius R_0 that is submerged in a Newtonian liquid of density ρ and dynamic viscosity μ . Since the microbubble may initially be in a prestressed state we generally have

$$R_0 = R_{SF} + U_d, \quad (1)$$

where R_{SF} is the stress-free radius of the bubble and U_d is the amount of compression or expansion imposed initially on the stress-free state. We investigate the microbubble response to a disturbance imposed on the far field:

$$P'_\infty = P'_{st} + P'_{dist} = P'_{st} + P'_{st}\varepsilon \cos(\omega_f t'), \quad (2)$$

with P'_{st} , P'_{dist} denoting the dimensional undisturbed and disturbed pressure in the far field, respectively, and ε , ω_f the amplitude and angular frequency of the acoustic disturbance, respectively; throughout this paper primed letters signify dimensional variables. We assume negligible compressibility of the surrounding liquid and a vanishing liquid velocity in the far field. The characteristic length scale is determined by the initial radius R_0 of the bubble, whereas the appropriate timescale is introduced via the external frequency as $1/\omega_f$. In this context, the characteristic velocity and pressure scales are expressed via quantities $\omega_f R_0$ and $\rho \omega_f^2 R_0^2$, respectively. When simulations of a coated microbubble that pulsates in response to a static overpressure are performed, the

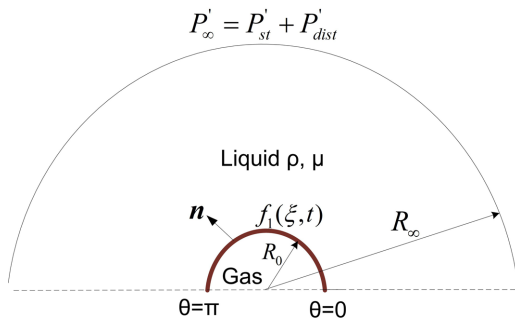


FIG. 1. A contrast agent in an unbounded flow.

eigenfrequency for volume pulsations, ω_0 , is used as characteristic timescale instead,

$$\omega_0 = \left(\frac{1}{\rho R_0^3} [3\gamma(2\sigma + P_{st}R_0) - 2\sigma + 4\chi] \right)^{1/2} \approx 2\pi \times 10^6 \text{ 1/s}, \quad (3)$$

corresponding to a microbubble with area dilatation modulus $\chi = 0.24 \text{ N/m}$; see also [16].

The problem formulation of a contrast agent in an unbounded flow is described via a spherical coordinate system and is given in detail in [16]. In order to obtain the governing equations, we assume axisymmetric variations of the bubble shape as well as the liquid velocity and pressure. In Fig. 1 a schematic representation of the flow under consideration is provided with f_1, R_∞ denoting the r-spherical coordinate of the thin shell that coats the bubble and the far field, respectively. Herein we focus on an unbounded flow domain in an attempt to identify the mechanism that controls the onset of compression-only behavior, leaving simulations of a wall-bounded flow arrangement for a future study.

The flow in the surrounding liquid is governed by the mass conservation and momentum equations expressed through the Navier-Stokes equations. Since the liquid is considered incompressible the governing equations for the liquid read in dimensionless form

$$\nabla \cdot \mathbf{u} = 0, \quad (4)$$

$$\frac{\partial \mathbf{u}}{\partial t} + (\mathbf{u} \cdot \nabla) \mathbf{u} = -\nabla P + \frac{1}{\text{Re}} \nabla \cdot \underline{\underline{\boldsymbol{\tau}}}, \quad \underline{\underline{\boldsymbol{\sigma}}} = -P \underline{\underline{\mathbf{I}}} + \frac{1}{\text{Re}} \underline{\underline{\boldsymbol{\tau}}}, \quad \underline{\underline{\boldsymbol{\tau}}} = \nabla \mathbf{u} + \nabla \mathbf{u}^T, \quad (5)$$

where $\mathbf{u} = (u_r, u_\theta, 0)$, $\text{Re} = (\rho \omega_f R_0^2) / \mu$ is the Reynolds number of the surrounding liquid flow that compares inertia with viscous forces, $\underline{\underline{\boldsymbol{\sigma}}}, \underline{\underline{\boldsymbol{\tau}}}$, the full and deviatoric stress tensors in the surrounding fluid, and $\underline{\underline{\mathbf{I}}}$ the unit tensor.

For the interface we employ a Lagrangian representation by introducing a Lagrangian coordinate ξ ($0 \leq \xi \leq 1$), which identifies the interfacial particles with $\xi = 0$ and $\xi = 1$ corresponding to the south ($\theta = \pi$) and north ($\theta = 0$) pole of the bubble, respectively. The force balance on the gas-liquid interface reads in dimensionless form

$$\left(-P \underline{\underline{\mathbf{I}}} + \frac{1}{\text{Re}} \underline{\underline{\boldsymbol{\tau}}} \right) \cdot \mathbf{n} + P_G \mathbf{n} = -\nabla_s \cdot (\underline{\underline{\boldsymbol{\tau}}} + q \mathbf{n}) + \frac{2k_m}{\text{We}} \mathbf{n} = \Delta \mathbf{F} + \frac{2k_m}{\text{We}} \mathbf{n}, \quad (6)$$

where \mathbf{n} denotes the unit normal vector pointing towards the surrounding fluid, P_G is the gas pressure inside the bubble, ∇_s, k_m signify the surface gradient and mean curvature of the bubble interface, respectively, and $\text{We} = \frac{\rho \omega_f^2 R_0^3}{\sigma}$ is the Weber number comparing inertia with capillary forces. Despite the viscoelastic nature of the shell a certain amount of surface tension, $\sigma = 0.051 \text{ N/m}$, is typically assumed for the lipid shells [7,8,17,18] as a measure of the internal gas exposure to the surrounding liquid, whereas for polymeric shells surface tension is set to zero. Finally, $\Delta \mathbf{F}$ is

the resultant force due to the viscoelastic properties of the membrane which, according to the theory of elastic shells, is derived by taking the surface divergence of the viscoelastic tension tensor on the membrane surface and is calculated as

$$\Delta \mathbf{F} = \left[k_s \tau_s + k_\phi \tau_\phi - \frac{1}{r_o} \frac{\partial}{\partial S} (r_o q) \right] \mathbf{n} - \left[\frac{\partial \tau_s}{\partial S} + \frac{1}{r_o} \frac{\partial r_o}{\partial S} (\tau_s - \tau_\phi) + k_s q \right] \mathbf{e}_s, \quad (7)$$

with S denoting the arclength of the interface, τ_s, τ_ϕ the principal elastic tensions, k_s, k_ϕ the two principal curvatures, $r_o = r \sin \theta$ the cylindrical polar coordinate and \mathbf{e}_s the tangential unit vector. In Eq. (7) q corresponds to the transverse shear tension that is obtained from a torque balance on the shell [19,20]:

$$q = \frac{K_B}{r_o} \frac{\partial r_o}{\partial S} \left[\frac{\partial}{\partial r_o} (r_o m_s) - m_\phi \right], \quad (8)$$

where m_s, m_ϕ express the principal bending moments and $K_B = k_B / (\rho \omega_f^2 R_0^5)$ signifies the relative importance of bending with respect to inertia.

The membrane tensions consist of an elastic and a viscous component,

$$\tau_s = \tau_{el} + \tau_v. \quad (9)$$

The membrane and bending stresses are defined via the shell constitutive laws; see also [15,16]. In particular, for the elastic part of the phospholipid shells we adopt the Mooney-Rivlin (MR) model [21] and for the polymeric shells we introduce Hook's law:

$$\tau_{el}^{MR} = \frac{G}{3\lambda_s \lambda_\phi} \left(\lambda_s^2 - \frac{1}{(\lambda_s \lambda_\phi)^2} \right) [1 + b(\lambda_\phi^2 - 1)], \quad (10a)$$

$$\tau_{el,s}^H = G \frac{[\lambda_s^2 - 1 + \nu(\lambda_\phi^2 - 1)]}{2(1 - \nu^2)\lambda_\phi}, \quad (10b)$$

with λ_s, λ_ϕ corresponding to the principal extension ratios based on the stress-free state, $G = \chi / (\rho \omega_f^2 R_0^3)$ signifying the relative importance of shell dilatation with respect to inertia and ν the Poisson ratio set to 0.5. The MR constitutive law is employed in order to describe shell softening during expansion. In contrast with our previous studies [16,22,23] the dilatational μ_s and the shear viscosity μ_{sh} of the shell are treated separately. More specifically, the viscous component is defined by

$$\tau_s^v = \left(\frac{1}{\text{Re}_s} + \frac{1}{\text{Re}_{sh}} \right) \frac{1}{\lambda_s} \frac{\partial \lambda_s}{\partial t} + \left(\frac{1}{\text{Re}_s} - \frac{1}{\text{Re}_{sh}} \right) \frac{1}{\lambda_\phi} \frac{\partial \lambda_\phi}{\partial t}, \quad (11)$$

with $\text{Re}_s = \rho \omega_f R_0^3 / \mu_s$ and $\text{Re}_{sh} = \rho \omega_f R_0^3 / \mu_{sh}$ comparing the inertia forces with the viscous dilatational and shear forces of the shell, respectively. As the shear viscosity, μ_{sh} , increases shape modes are damped faster as the shell deforms. Shell viscosities μ_s, μ_{sh} (SI units in kg/s) are related to the 3D shell viscosity $\mu_{s,3d}, \mu_{sh,3d}$ (SI units in Pa s) via $\mu_s = 3\delta \mu_{s,3d}$ where δ is the shell thickness.

Besides the force balance, continuity of the liquid and shell velocities on the interface read as

$$\mathbf{u} = \frac{D\mathbf{r}_s}{Dt} \quad (12)$$

with \mathbf{r}_s denoting the position vector of a particle at the interface.

At equilibrium, the dimensionless pressure, P_G , inside the bubble is related to the dimensionless pressure, P_{st} , on the far field as follows:

$$P'_G(t' = 0) = P'_{st} + \frac{2\sigma}{R_0} + \frac{2}{R_0} \frac{\chi}{3} \left[1 - \left(\frac{R_{SF}}{R_0} \right)^6 \right] \quad (13a)$$

$$\rightarrow P_G(t = 0) = P_{st} + \frac{2}{W_e} + 2\tau_{el}(t = 0). \quad (13b)$$

When there is gas leakage through the shell prior to the acoustic disturbance, a dimensionless initial overpressure is established, $\Delta P_{\text{ps}} \equiv (P'_{\text{st}} - P'_G[t' = 0])/P'_{\text{st}}$, that determines the initial compression of the microbubble, R_0/R_{SF} , based on static shell equilibrium, Eq. (6), assuming spherosymmetry:

$$R_{\text{ps}} \equiv \frac{R_0}{R_{\text{SF}}} = F\left(\frac{P'_{\text{st}} - P'_G(t' = 0)}{P'_{\text{st}}}\right) = F(\Delta P_{\text{ps}}). \quad (14)$$

In order to determine the pressure inside the bubble the assumption of uniformity due to negligible density and kinematic viscosity of the enclosed gas is made. Moreover, bubble oscillations are characterized as nearly isothermal since heat transfer between the bubble and the surrounding liquid is assumed to take place fast in comparison with the timescale of the phenomena under consideration. In this context, the bubble pressure is given by

$$P_G(t = 0)V_G^\gamma(t = 0) = P_G(t)V_G^\gamma(t) = \text{const}, \quad (15)$$

with V_G denoting the dimensionless instantaneous volume of the bubble, $V_G(t = 0) = \frac{4\pi}{3}$ the initial volume of the bubble, and γ the polytropic constant set to 1.07 for an almost isothermal variation. The latter value is also close to the ratio of specific heats of certain ideal gases that are carried by known contrast agents and undergo adiabatic pulsations during insonation [3,7,8].

III. STABILITY ANALYSIS

A. Static stability analysis

As was stressed in the introduction section, lipid-coated microbubbles are observed to pulsate around a compressed and deformed state instead of the initial spherical configuration, and this dynamic response pattern is often called ‘‘compression-only’’ pulsation. Since coated microbubbles are also known [14,16,24] to possess a rich bifurcation diagram that contains significantly compressed states due to their compressibility and shell elasticity, it is important to establish a potential association between these two aspects of their static and dynamic response. To this end, we perform a systematic analysis of the static configuration of lipid and polymeric microbubbles aiming at the construction of bifurcation diagrams for a parameter range, in terms of size, area dilatation and bending moduli, that is relevant to available acoustic measurements. The numerical methodology closely follows the analysis presented by Lytra and Pelekasis [14,25]. It entails solution of the formulation presented in the previous section setting the fluid and interfacial velocity to zero. Numerical solution was performed via the Galerkin Finite Element Methodology that employs 1D cubic splines for the description of the bubble shape. These basis functions satisfy continuity of the second derivative and this facilitates treatment in the weak formulation of bending stresses which involve fourth-order derivatives. The nonlinearity of the problem is treated with the Newton-Raphson method with the determinant of the Jacobian providing the bifurcation points when it crosses from positive to negative values and vice versa. The calculated eigenvector corresponding to a vanishing eigenvalue provides the details of the emerging branch in the vicinity of the bifurcation point. In this fashion, previously obtained bifurcation diagrams are extended and complemented to accommodate the needs of the present study. Evolution of the obtained static equilibrium as the external overpressure varies is captured via simple or arc-length continuation in portions of the solution branch where the determinant of the Jacobian is nonzero and around limit points, respectively. As postprocessing of the numerical process the total energy of the microbubble, accounting for shell elastic energy in terms of stretching and bending and the energy due to volume compression and surface tension, is calculated and compared among different solutions obtained for the same shell parameters. The bifurcation diagrams for the cases we examine are given in Sec. VA in the $(V/V_0, \varepsilon)$ plane, with V_0 denoting the initial bubble volume and $\varepsilon = \Delta P/P'_{\text{st}} = (P'_\infty - P'_{\text{st}})/P'_{\text{st}}$, the dimensionless external overpressure as a function of the dimensionless bending resistance, $k_B/(\chi R_0^2)$, and dimensionless initial overpressure, ΔP_{ps} .

B. Parametric stability analysis

When they are subject to a large enough far-field overpressure coated microbubbles tend to eventually acquire deformed shapes that are energetically favored, among the ones predicted by the bifurcation diagram corresponding to the shell parameters. As a result, growth of the dominant shape modes occurs spontaneously albeit on a much larger timescale in comparison with the natural frequency for volume pulsation [16], when they are absent from the initial microbubble shape, e.g., when the initial bubble shape is spherical. However, this process can be significantly accelerated through parametric shape mode excitation when an acoustic disturbance is imposed in the far field, provided the amplitude and frequency of the disturbance in conjunction with the shell viscoelastic properties allow for such a transition to take place. Tsiglifis and Pelekasis [15] performed stability analysis for the spherosymmetric pulsations of a contrast agent that is excited acoustically with small axisymmetric disturbances. In this fashion, they obtained phase diagrams illustrating the amplitude threshold for parametric mode excitation and dynamic buckling (DB) to occur, as a function of microbubble rest radius for fixed forcing frequency and shell properties. Dynamic buckling refers to a Rayleigh-Taylor-type instability that occurs very fast during the rebound phase of the radial pulsation following maximal volume compression, that triggers loss of shell cohesion. When the amplitude threshold for parametric instability is sufficiently below the one for DB saturated pulsations around a deformed shape are possible and this bears significance to the onset of compression-only behavior of coated microbubbles. In the present article the analysis by Tsiglifis and Pelekasis is extended and enriched with features that affect the emergence of parametric mode excitation. In particular, we will examine the manner in which the stability of contrast agents is affected when the disparity between area dilatation and bending modulus or between shear and dilatational viscosity increases. Coupling the above effects with the situation where the shell is initially at a prestressed state, possibly due to gas leakage through the shell, offers additional possibilities for shell destabilization. Since the detailed stability analysis is given in [15], in the present study we only present a brief description of the analysis and focus mainly on the impact of additional features such as prestress and the disparity between shear and dilatational viscosity, in the interest of brevity.

We perturb the base state of the system that corresponds to the microbubble performing radial pulsations due to an acoustic disturbance that is imposed in the far field. Upon assuming incompressible flow and neglecting viscous dissipation in the surrounding liquid in comparison with shell viscosity [26] the zeroth-order problem is recovered that consists of a modified Rayleigh-Plesset equation describing the instantaneous radial position \hat{R} of the shell in response to the far-field pressure $P_\infty(t) = P_{st} + \varepsilon \cos t$:

$$\begin{aligned} \hat{R} \ddot{\hat{R}} + \frac{3}{2} \dot{\hat{R}}^2 &= P_G(t) - \frac{2k_m^0}{\hat{W}e} - \Delta F_n^0 - P_\infty(t), \quad \hat{R}(t) \equiv R'/R_{SF}, \\ \hat{R}(0) = R_0/R_{SF} = R_{ps} &= 1 + \frac{U_d}{R_{SF}} \xrightarrow{U_d < 0} R_{ps} < 1, \quad \dot{\hat{R}}(t=0) = 0 \end{aligned} \quad (16)$$

with the gas pressure $P_G(t)$ provided by Eq. (15), ΔF_n^0 signifying the zeroth-order normal component of the force due to shell viscoelasticity, $k_m^0 = 1/\hat{R}$ the instantaneous dimensionless mean curvature of the pulsating microbubble while R_{ps} is a measure of the shell prestress that depends on the initial dimensionless overpressure ΔP_{ps} . The stress-free radius, R_{SF} , is employed as a characteristic length scale rather than the initial bubble radius, R_0 , in order to conform with the analysis in Ref. [15]; $\hat{W}e$ is also defined via the stress-free radius in this context. Upon expanding in the sound amplitude ε and linearizing, the natural frequency for volume pulsation is obtained in the form of Eq. (3). In the present study we are interested in obtaining the amplitude threshold for growth of shape modes, therefore we investigate the microbubble response to disturbances involving axisymmetric shape modes for arbitrarily large sound amplitude ε . To this end we examine the dynamics of the microbubble in response to infinitesimal disturbances in the bubble shape, scaled

via dimensionless parameter $\hat{\varepsilon} \ll 1$, involving axisymmetric shape modes:

$$r = \hat{R}(t) + \hat{\varepsilon}w, \quad \theta = \theta_0 + \hat{\varepsilon}u/\hat{R}(t), \quad (17)$$

with $w(\theta_0)$, $u(\theta_0)$, denoting the displacements along the radial and azimuthal directions, respectively, and θ_0 , the azimuthal angle along the generating curve of the spherosymmetric stress-free shape. Following Tsiglifs and Pelekasis [15] we expand w and u in terms of the Legendre polynomials P_n which constitute the eigenfunctions of the problem in the azimuthal direction,

$$w = \sum_{n=1}^{\infty} w_n(t)P_n(\theta_0), \quad \psi = \sum_{n=1}^{\infty} \psi_n(t)P_n(\theta_0), \quad u \equiv \frac{d\psi}{d\theta_0}, \quad (18a)$$

and recover, to first order in $\hat{\varepsilon}$, the time evolution of the coefficients of the different shape modes in the manner obtained in the latter study:

$$\begin{aligned} \ddot{w}_n + \frac{3\dot{\hat{R}}}{\hat{R}}\dot{w}_n + \left[\frac{(1-n)\ddot{\hat{R}}}{\hat{R}} + \frac{(n+1)(n-1)(n+2)}{\hat{W}e\hat{R}^3} \right] w_n \\ + \frac{n+1}{\hat{R}}\Delta F_n^1(\dot{w}_n, \dot{\psi}_n, w_n, \psi_n, \hat{B}, \hat{G}, \hat{W}e, \hat{R}e_s, \hat{R}e_{sh}, R_{ps}, \hat{R}, \dot{\hat{R}}, n) = 0, \end{aligned} \quad (18b)$$

$$\Delta F_t^1(\dot{w}_n, \dot{\psi}_n, w_n, \psi_n, \hat{B}, \hat{G}, \hat{W}e, \hat{R}e_s, \hat{R}e_{sh}, R_{ps}, \hat{R}, \dot{\hat{R}}, n) = 0, \quad (18c)$$

where $\hat{B} = k_B/(\chi R_{SF}^2)$, $\hat{G} = \chi/\rho\omega_f^2 R_{SF}^3$, $\hat{R}e_s = \rho\omega_f R_{SF}^3/\mu_s$, $\hat{R}e_{sh} = \rho\omega_f R_{SF}^3/\mu_{sh}$, $\hat{W}e = \rho\omega_f^2 R_{SF}^3/\sigma$. The exact form of the normal and tangential stress components ΔF_n^1 , ΔF_t^1 is given in detail in [15] and is modified here in order to account for prestress R_{ps} and the difference in shear and dilatational viscosities μ_{sh} , μ_s . The respective forms are provided in the Appendix of the present study. Equations (18) are solved for a given initial deviation from sphericity, $w_n(t=0)$, $\psi_n(t=0)$, and a radial history, $\hat{R}(t)$, provided by Eq. (16) and the appropriate initial conditions. When $|w_n(t)|$, $|\psi_n(t)|$ exhibit growth within 30 periods of the forcing, ω_f , the n th Legendre mode is considered as parametrically unstable, whereas when $|w_n(t)|$, $|\psi_n(t)|$ become comparable with the microbubble instantaneous radius $\hat{R}(t)$ within 10 periods of the forcing the dynamic response is identified as DB leading to loss of microbubble cohesion. The former response type is captured for a lower sound amplitude and is categorized as parametric instability that can potentially generate a ‘‘compression-only’’ behavior, when the n th mode corresponds to the one dominating the buckled shapes captured in the static bifurcation diagrams presented in Sec. VA 1.

IV. NUMERICAL METHODOLOGY

Based on the problem formulation of Sec. II we also perform numerical simulations of freely pulsating microbubbles in response to a step change or an acoustic disturbance, in order to investigate their dynamic response leading to the onset of saturated pulsations. The possibility for pulsation around a compressed state is investigated in order to provide a mechanism for compression-only response to emerge. The numerical methodology proposed by Vlachomitrou and Pelekasis [16] is implemented with a superparametric finite element formulation involving the standard biquadratic/bilinear representation for the unknown velocity and pressure fields coupled with the B-cubic splines for the unknown location of the bubble-liquid interface. The introduction of cubic splines is necessary because a fourth-order derivative arises in the force balance equation [Eq. (6)] through the bending resistance of the shell. The continuity of the velocity components is imposed as an essential boundary condition on the interface, whereas the normal and tangential force balances are employed and discretized using the 1D cubic splines as bases functions in order to determine the two coordinates $r(\xi, t)$ and $\theta(\xi, t)$ of the shape of the microbubble. On the far field, which is considered to be 10 rest radii away from the bubble centroid, the imposed pressure disturbance is prescribed, while the velocity components are set to zero. The fully implicit Euler

scheme is introduced for the temporal integration and the nonlinearity of the problem is treated with the Newton-Raphson method.

The mesh is dynamically adapted once the interface is updated, using the elliptic mesh generation scheme. According to the employed method the coordinates of the grid points in the physical domain are defined by solving the following set of partial differential equations [27,28]:

$$\nabla \cdot \left(\varepsilon_1 \sqrt{\frac{r_\xi^2 + z_\xi^2}{r_\eta^2 + z_\eta^2}} + 1 - \varepsilon_1 \right) \nabla \xi = 0, \quad (19)$$

$$\nabla \cdot \nabla \eta = 0. \quad (20)$$

These equations are discretized using the biquadratic Lagrangian basis functions and the integral terms that the divergence theorem produces are omitted to weakly impose orthogonality of the grid lines in the boundaries. Introduction of the term $\sqrt{\frac{r_\xi^2 + z_\xi^2}{r_\eta^2 + z_\eta^2}}$ in the first equation allows the η curves to intersect the interface almost orthogonally, while ε_1 is an empirical parameter that ranges between 0 and 1 and controls the extent of mesh smoothness versus its orthogonality. Its value in each problem is defined by trial and error and in our case is set to 0.1. The second equation generates the ξ curves which are nearly parallel to the interface and are constructed so that they follow its deformation. In any boundary where the coordinate is known, the corresponding equation for the grid is not written. Instead, the value of the coordinate is imposed as an essential boundary condition.

The validation of the numerical methodology adopted in this paper, with or without wall interaction, was thoroughly presented in Vlachomitrou and Pelekasis [16,22] with several benchmark tests.

V. RESULTS AND DISCUSSION

Before we proceed to discuss the results of the dynamic numerical simulations it is crucial to examine the encapsulated microbubbles we consider theoretically, in terms of static stability analysis and parametric stability analysis. This will help us interpret the numerical results and establish a potential association between their dynamic and static response.

Bubbles with soft lipid shells obeying the Mooney-Rivlin constitutive law and hard polymeric shells following the standard neo-Hookean behavior are studied in an effort to capture the different response patterns reported in the literature. More specifically, for the lipid-shelled contrast agents we consider a stress-free radius $R_{SF} = 3.6 \mu\text{m}$, thickness $\delta = 1 \text{ nm}$, bending modulus $k_B = 3 \times 10^{-14} \text{ Nm}$ and we employ the Mooney-Rivlin constitutive law with the degree of softness b set to zero [3,21]. Three different cases for the area dilatational modulus are examined: $\chi = 0.12 \text{ N/m}$, $\chi = 0.24 \text{ N/m}$, and $\chi = 0.48 \text{ N/m}$. The dilatational shell viscosity is set to $60 \times 10^{-9} \text{ kg/s}$, whereas the shear shell viscosity varies from $3 \times 10^{-9} \text{ kg/s}$ to $60 \times 10^{-9} \text{ kg/s}$ (μ_{sh}/μ_s varies from 0.05 to 1). For the polymeric shell we consider the PB-127 microbubble with a stress-free radius of $R_{SF} = 2 \mu\text{m}$, $\delta = 15 \text{ nm}$ thickness, area dilatation modulus $\chi = 9 \text{ N/m}$ and a bending modulus equal to $k_B = 2.25 \times 10^{-16} \text{ Nm}$. The dilatational viscosity is set to $45 \times 10^{-9} \text{ kg/s}$, whereas the shear viscosity varies from $2.25 \times 10^{-9} \text{ kg/s}$ to $45 \times 10^{-9} \text{ kg/s}$ (μ_{sh}/μ_s varies again from 0.05 to 1). The selection of the area dilatational modulus, the shell thickness and the dilatational shell viscosity was based on typical shell viscoelastic properties that have been estimated in experimental studies [8,9,29–31] and previously employed for the analysis and simulations of coated microbubbles; e.g., see [14–16,22,23,26].

In view of previous reports of gas leakage between acoustic measurements of coated microbubbles and the resulting onset of shape deformation at relatively small sound amplitudes [6–10], in the present study emphasis is placed on the effect of prestress on the dynamic response of the microbubble by effecting the onset of deformation and buckling at significantly lower amplitudes.

This is the opposite effect to the swelling that is often observed with artificial capsules in response to the osmotic pressure that develops when they are suspended in a saline solution [32], which has a stabilizing impact on buckling. In order to facilitate comparison between shapes registered in bifurcation diagrams (Sec. V A 1) using static analysis and the dynamic response pattern captured for prestressed initial conditions, in the latter case we carry out parametric stability analysis and perform simulations. We employ an initially compressed bubble radius R_0 that is related with the stress-free radius, R_{SF} , via Eq. (1) with the initial radial displacement U_d taken to be negative corresponding to a compressed state. As was already pointed out, initial compression is assumed to be a result of gas leakage through the shell before the acoustic disturbance is applied, while the far-field pressure remains constant, $P'_\infty = P'_{st}$; see Eq. (14). In this case the initial radius R_0 is taken to be slightly larger than the critical radius R_B for static buckling to take place. Then a step change or an acoustic disturbance is applied of the form shown in Eq. (2) corresponding to a vanishing or finite forcing frequency, respectively.

The amplitude ε of the disturbance is selected so that it lies beyond the threshold for the onset of static buckling registered in the bifurcation diagrams constructed in Sec. V A 1 for a prestressed microbubble with the same amount of prestress, U_d/R_{SF} , and viscoelastic properties; i.e., $R_{SF} > R_0 > R_B$.

A. Stability

1. Construction of bifurcation diagrams

As will also be discussed in the following analysis, in order to assist interpretation of and detailed comparison with numerical simulations of prestressed microbubbles performed in the present study, the bifurcation diagrams obtained herein pertain to shells that are prestressed. As a result, the calculated equilibrium branches differ from those obtained by Lytra and Pelekasis [14] but retain their original qualitative features. More specifically, Figs. 2–5 illustrate the features of the static response of coated microbubbles for a strain-softening shell with progressively larger area dilatation χ (Figs. 2–4) and a hard polymeric shell that exhibits neo-Hookean behavior (Fig. 5). Bifurcation diagrams obtained for an initially prestressed shell are provided, followed by the shape evolution in the emerging solution branches that invariably produce significantly compressed shapes as their deviation from sphericity increases. The branches are named after the Legendre mode that arises at the bifurcation point. P_n refers to the n th Legendre mode and the interfacial shape is illustrated in terms of the Cartesian coordinates $z_B = r\cos\theta$ and $x = r\sin\theta$ where r , θ , φ , signify spherical coordinates with θ , φ denoting the azimuthal and polar angles; coordinate z_B is measured with respect to the geometric center of the bubble and is aligned with the axis of symmetry.

Figures 2–5 portray the evolution of the bifurcation diagram for decreasing relative bending resistance of the shell, $\hat{B} = k_B/(\chi R_{SF}^2)$, indicating a progressive hardening of the shell material. As far as the lipid shells are concerned (Figs. 2–4), it is clear that the bifurcation branches correspond to low shape modes whereas as the shell becomes harder (Fig. 4) higher modes appear as well. In terms of amplitude, for the softer shell with $\chi = 0.12$ N/m (Fig. 2) the symmetric mode P_2 develops first ($\varepsilon_{P_2} \approx 0.08$) and modes P_3 ($\varepsilon_{P_3} \approx 0.169$) and P_4 ($\varepsilon_{P_4} \approx 0.445$) follow. For the shell with $\chi = 0.24$ N/m (Fig. 3) the asymmetric mode P_3 ($\varepsilon_{P_3} \approx 0.031$) emerges first and shortly after modes P_2 ($\varepsilon_{P_2} \approx 0.09$) and P_4 ($\varepsilon_{P_4} \approx 0.174$) appear, whereas when the area dilatational modulus is set to $\chi = 0.48$ N/m we have four bifurcation branches: P_3 ($\varepsilon_{P_3} \approx 0.12$), P_2 ($\varepsilon_{P_2} \approx 0.163$), P_5 ($\varepsilon_{P_5} \approx 0.311$), and P_4 ($\varepsilon_{P_4} \approx 0.375$). Finally, in Fig. 5 that corresponds to a polymeric shell, the bifurcation branches correspond to high modes P_{19} and P_{20} ($\varepsilon_{P_{19}} \approx 8.9 \times 10^{-2}$ and $\varepsilon_{P_{20}} \approx 9 \times 10^{-2}$) reflecting intense shell hardening.

In all cases the branches exhibit bifurcation points. Branches characterized by the same mode develop transcritically with oblate and prolate shapes; see, for example, P_2 or P_4 in Fig. 2(a). Subcritical branches exhibit limit points that lead the solution development towards higher dimensionless overpressure, P_2 oblate or P_4 oblate, while supercritical branches develop monotonically, like the P_3 in the same figure. The shapes eventually develop contact areas for smaller amplitudes

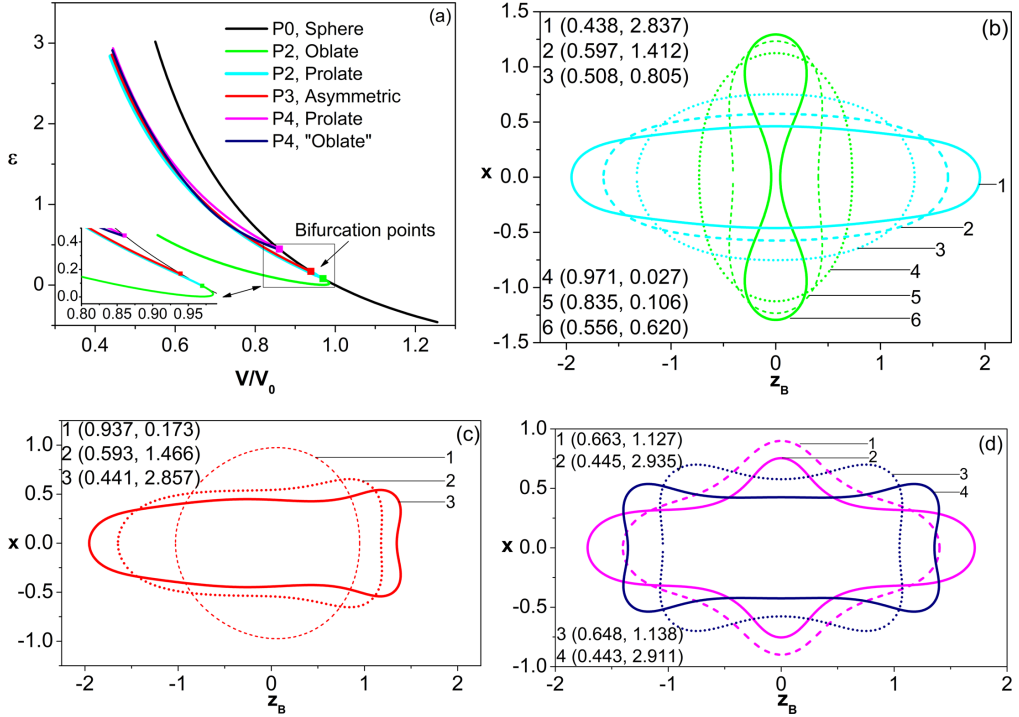


FIG. 2. (a) Bifurcation diagram for a lipid-coated microbubble, embedded graph shows details around the bifurcation points, and (b)–(d) shape of the microbubble corresponding to P₂ oblate and prolate, P₃ asymmetric and P₄ oblate and prolate branches, respectively, for selected points on the bifurcation diagram ($V/V_0, \varepsilon$); $\chi = 0.12$ N/m, $k_B = 3 \times 10^{-14}$ N m, $U_d = -0.61 \mu\text{m}$, $R_{\text{SF}} = 3.6 \mu\text{m}$; $R_{\text{ps}} = R_0/R_{\text{SF}} \approx 0.83$, $\hat{B} = k_B/(\chi R_{\text{SF}}^2) \approx 0.02$.

in comparison with branches obtained without prestress. Shapes indicated with negative amplitude pertain to the part of the solution branch that evolves towards lower amplitudes below the original bifurcation point. The shapes presented in Figs. 2–5 along with their level of compression and dominant shape modes will be used in order to assist the interpretation of dynamic patterns in the acoustic response of prestressed microbubbles obtained by our simulations presented in Sec. V B. Hence, a more detailed discussion on the above bifurcation diagrams is postponed until a latter section.

2. Parametric stability analysis

Phase diagrams are also constructed for shells exhibiting the amount of prestress for which bifurcation diagrams were obtained in Sec. V A 1 and varying the ratio of shear to dilatational viscosity of the shell, μ_{sh}/μ_s . Thus, the amplitude threshold for the different shape modes to emerge via parametric instability or DB is illustrated, along with the static buckling thresholds for the branches that bifurcate from the main spherically symmetric branch. The latter are shown as horizontal lines since they do not depend on shell viscosity. In particular, Figs. 6–9 provide the phase diagrams for the shells whose bifurcation diagrams are provided in Figs. 2–5. Figures 7(b) and 9(d) provide the phase diagram for varying discrepancy between shear and dilatational shell viscosity in the absence of initial prestress for a lipid and a polymeric shell, in order to stress the impact of prestress on shell stability.

By carefully examining these graphs, it is clear that the initial prestress reduces the static thresholds below the parametric excitation thresholds. This is most evident if we compare Fig. 7(a)

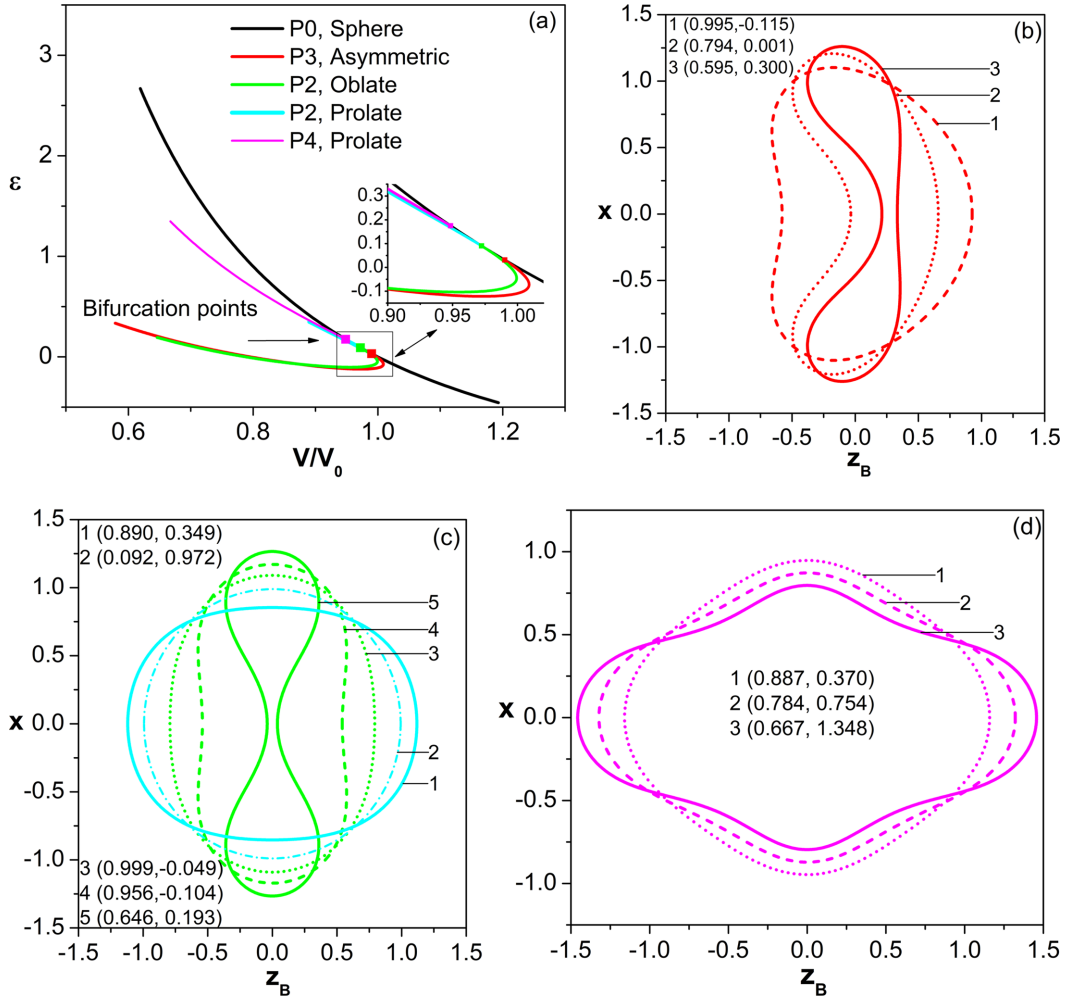


FIG. 3. (a) Bifurcation diagram for a lipid-coated microbubble, embedded graph shows details around the bifurcation points, and (b)–(d) shape of the microbubble corresponding to P₃ asymmetric, P₂ oblate, and prolate and P₄ prolate branches, respectively, for selected points on the bifurcation diagram (V/V_0 , ε); $\chi = 0.24$ N/m, $k_B = 3 \times 10^{-14}$ N m, $U_d = -0.46$ μ m, $R_{SF} = 3.6$ μ m; $R_{ps} \approx 0.872$, $\hat{B} \approx 0.01$.

that assumes an initial prestress state with Fig. 7(b) that corresponds to a stress-free initial condition [the same is also evident by comparing Fig. 9(c) to Fig. 9(d)]. In this fashion, a “window” is formed in sound amplitude where the dynamic and the static limits are well separated. However, as the shell becomes harder, this window becomes narrower, especially for polymeric shells (Fig. 9). In the latter case, not only the parametric shape mode excitation limits for many high modes are significantly low, but the dynamic bucking (DB) limit falls below the parametric thresholds and thus quick shell destabilization is expected. It is also clear that for lipid shells (Figs. 6–8) as the shear viscosity of the shell is reduced compared to the dilatational one, the parametric and DB limits decrease as well, whereas for polymeric shells (Fig. 9) the effect of the discrepancy nearly vanishes. In addition, when the ratio of the shear to dilatational shell viscosity is considerably small for lipid-shelled microbubbles the shape modes that are excited parametrically correspond to the modes of the bifurcation branches. The latter behavior is not observed for polymeric shells.

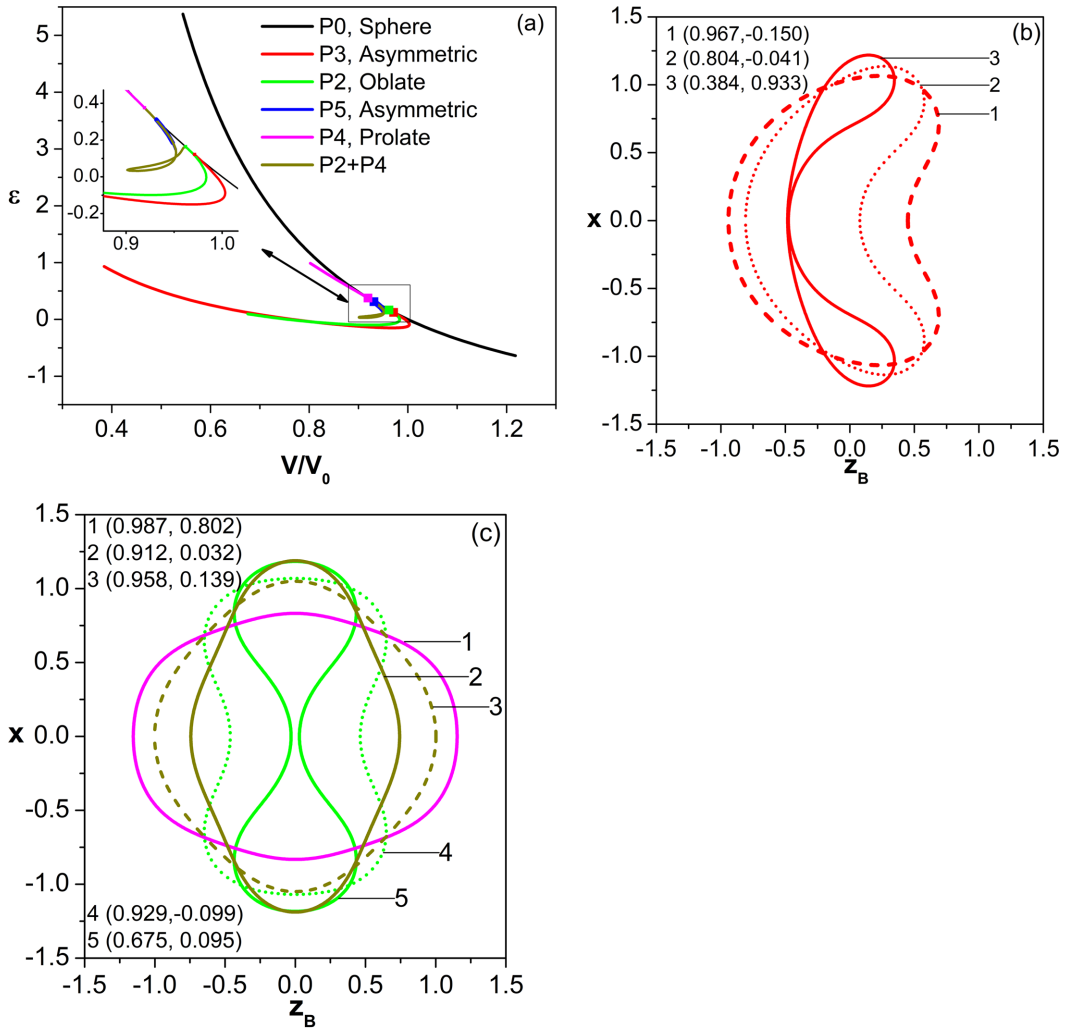


FIG. 4. (a) Bifurcation diagram for a lipid-coated microbubble, embedded graph shows details around the bifurcation points, (b) shape of the microbubble corresponding of P_3 asymmetric branch, and (c) corresponding shape of the merging branches P_2 and P_4 for selected points on the bifurcation diagram (V/V_0 , ϵ); $\chi = 0.48$ N/m, $k_B = 3 \times 10^{-14}$ N m, $U_d = 0.3 \mu\text{m}$, $R_{SF} = 3.6 \mu\text{m}$; $R_{ps} \approx 0.916$, $\hat{B} \approx 0.005$.

It should be pointed out that in carrying out the stability analysis liquid viscosity was neglected; see also [15]. Consequently, the produced phase diagrams only provide a general trend for the amplitude thresholds of the emerging shape modes. The latter will be underestimated in comparison with the simulations that account for viscous dissipation in the surrounding liquid. Furthermore, the effect of forcing frequency should be emphasized since a very small frequency will tend to reproduce the static buckling thresholds pertaining to a step change in the far-field pressure, whereas a large frequency will favor the predictions of the above phase diagrams corrected for the effect of liquid viscosity. In this context, dynamic simulations performed in the present study for freely pulsating bubbles will be employed in order to corroborate the above patterns and are presented in the following section. These effects will also be critical for the interpretation of numerical simulations that capture compression-only response of coated microbubbles pulsating in the vicinity of a rigid wall, but the latter simulations will be presented in a future study. In the present study we

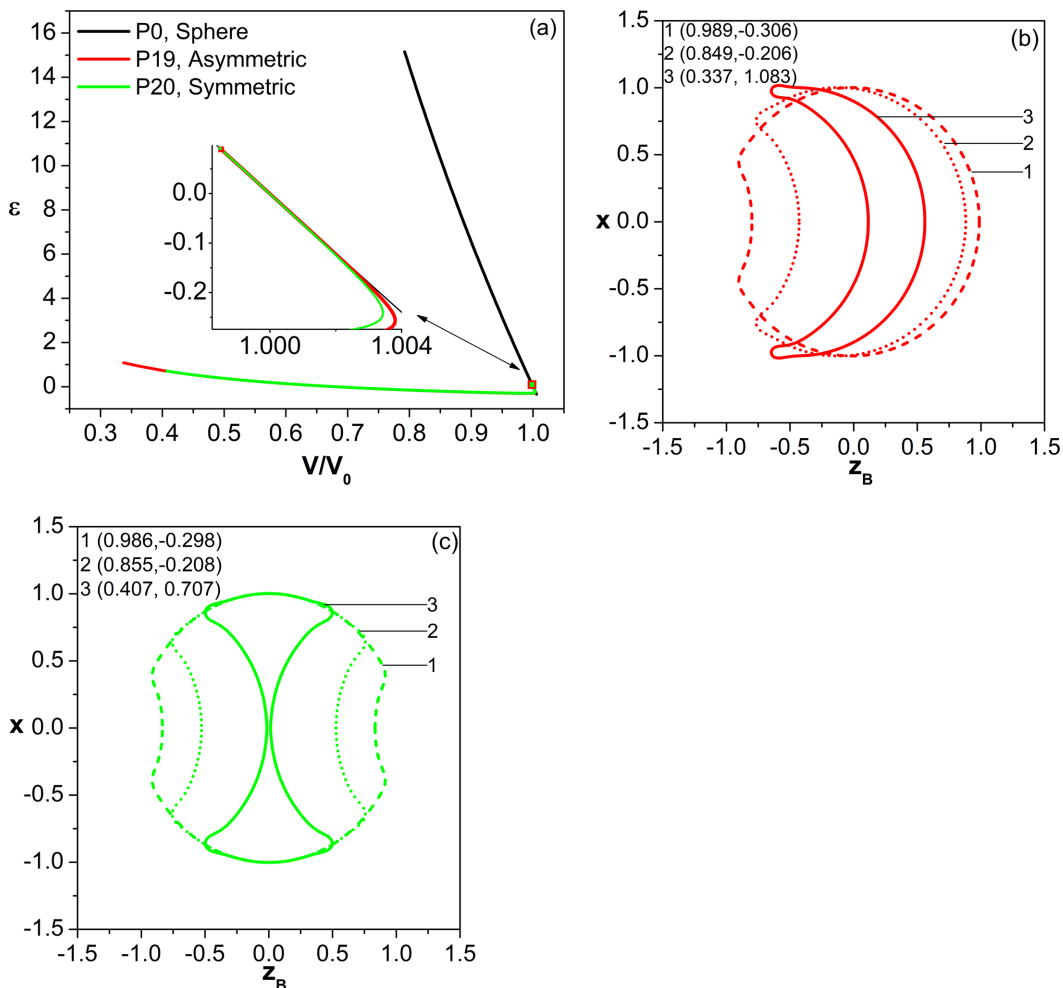


FIG. 5. (a) Bifurcation diagram for a polymer-coated microbubble ($\chi = 9$ N/m, $k_B = 2.25 \times 10^{-16}$ N m, $U_d = -0.004$ μ m, $R_{SF} = 2$ μ m, $\delta = 15$ nm) and (b, c) shapes of the microbubble corresponding to P₁₉ asymmetric and P₂₀ symmetric branches, respectively, for selected points on the bifurcation diagram ($V/V_0, \varepsilon$); embedded graph shows details around the bifurcation points; $R_{ps} \approx 0.999$, $\hat{B} \approx 6 \times 10^{-6}$.

are mainly interested in identifying the mechanism behind the onset of compression-only response, hence we extend the simulations over a large number of pulsations, ~ 50 , leaving the specification of time frame to the study that includes wall effects.

B. Dynamic simulations

In this section we proceed to present and discuss the results of the simulations performed with freely pulsating bubbles and examine them in the light of predictions by bifurcation diagrams and linear stability analysis obtained for the same shell parameters.

Dynamic simulations performed in [16] for an unbounded flow and a step change disturbance in the far-field pressure of amplitude $\varepsilon = 2$, captured the evolution of the interfacial shape until the bubble concludes to the static equilibrium. Figures 10(a) and 10(b) provide the temporal evolution of the bubble shape and breathing mode P_0 as well as the Legendre shape mode decomposition of the interface for this case. After the onset of static buckling the bubble temporarily achieves static

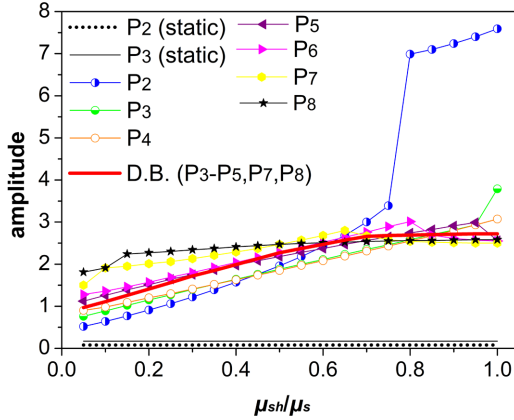


FIG. 6. Phase diagram with increasing μ_{sh}/μ_s ratio for a lipid-coated microbubble ($R_{SF} = 3.6 \mu\text{m}$, $\mu_s = 60 \times 10^{-9} \text{ kg/s}$, $\chi = 0.12 \text{ N/m}$, $k_B = 3 \times 10^{-14} \text{ N m}$, $\delta = 1 \text{ nm}$) subject to an initial prestress of $U_d = -0.61 \mu\text{m}$ and an acoustic disturbance of $f = 1.7 \text{ MHz}$; $R_{ps} \approx 0.83$, $\hat{B} \approx 0.02$, $\hat{R}e_s \approx 8.3$.

equilibrium with an oblate symmetric shape that is bent in the region around the two poles; see shape corresponding to $t = 88.4$ in Fig. 10(a) and mode saturation between $t = 75$ and $t = 90$ in Fig. 10(b). It should be noted that in panels illustrating the evolution of bubble shapes, the horizontal axis, z_B , corresponds to the axis of symmetry. As time evolves, this static shape is destabilized and the bubble, eventually, reaches another deformed equilibrium state that is asymmetric and is characterized by significant volume reduction and lower total energy content compared to the intermediate symmetric one. When the amplitude of the step change is reduced to $\varepsilon = 1.75$ the bubble bypasses the symmetric equilibrium and settles to a similar asymmetric equilibrium as the one shown in Fig. 10(a) on a similar time interval. Upon disturbing the same microbubble in terms of stress-free radius and viscoelastic properties, albeit at an initially compressed state with $U_d = -0.46 \mu\text{m}$ due to gas leakage and with an amplitude $\varepsilon = 0.3$, a dynamic response that is similar to the one illustrated in Figs. 10(a) and 10(b) is recovered, Figs. 10(c) and 10(d); the

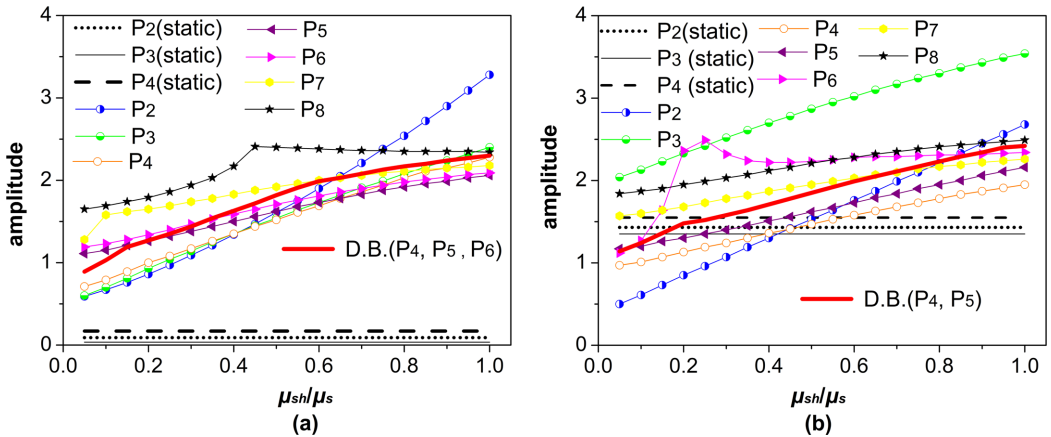


FIG. 7. Phase diagram with increasing μ_{sh}/μ_s ratio for a lipid-coated microbubble ($R_{SF} = 3.6 \mu\text{m}$, $\mu_s = 60 \times 10^{-9} \text{ kg/s}$, $\chi = 0.24 \text{ N/m}$, $k_B = 3 \times 10^{-14} \text{ N m}$, $\delta = 1 \text{ nm}$) subject to (a) an initial prestress of $U_d = -0.46 \mu\text{m}$, (b) no initial prestress, and an acoustic disturbance of $f = 1.7 \text{ MHz}$; $R_{ps} \approx 0.872$, $\hat{B} \approx 0.01$, $\hat{R}e_s \approx 8.3$.

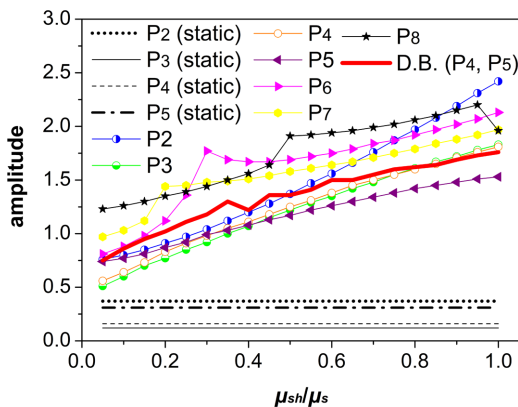


FIG. 8. Phase diagram with increasing μ_{sh}/μ_s ratio for a lipid-coated microbubble ($R_{SF} = 3.6 \mu\text{m}$, $\mu_s = 60 \times 10^{-9} \text{ kg/s}$, $\chi = 0.48 \text{ N/m}$, $k_B = 3 \times 10^{-14} \text{ N m}$, $\delta = 1 \text{ nm}$) subject to an initial prestress of $U_d = -0.3 \mu\text{m}$ and an acoustic disturbance of $f = 1.7 \text{ MHz}$; $R_{ps} \approx 0.916$, $\hat{B} \approx 0.005$, $\hat{R}e_s \approx 8.3$.

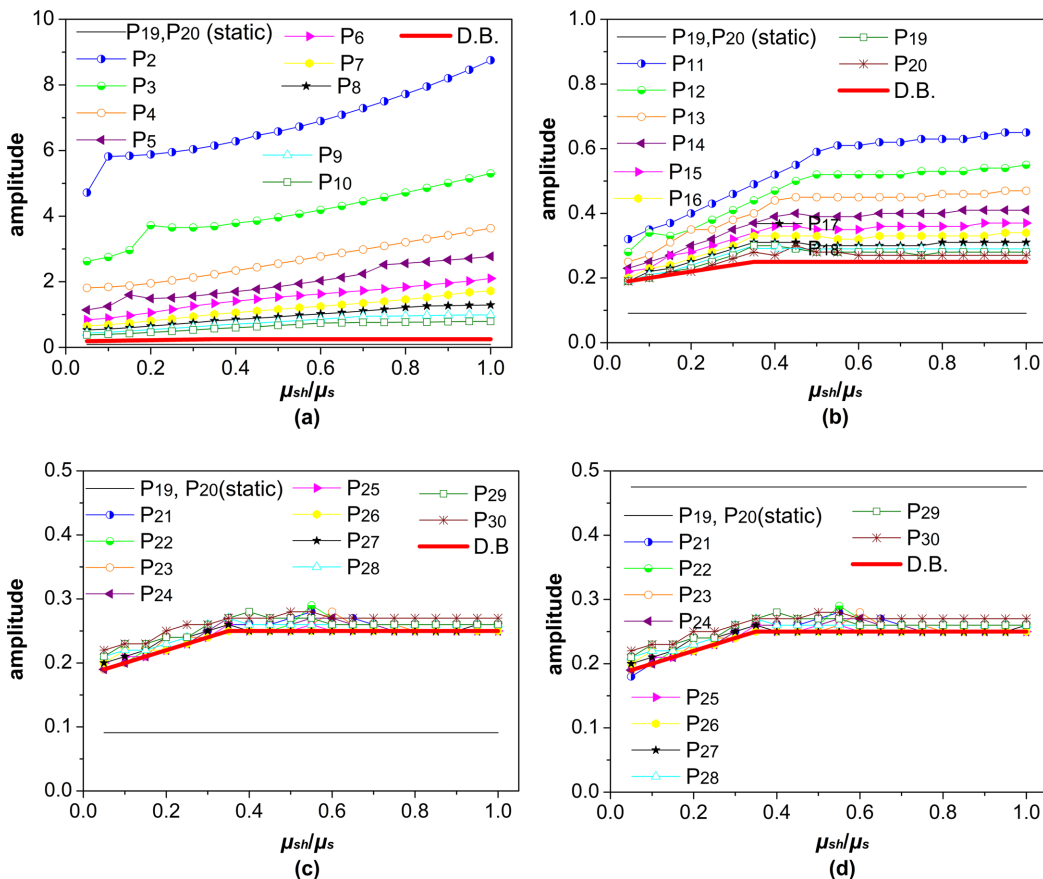


FIG. 9. Phase diagram with increasing μ_{sh}/μ_s ratio for a polymer-shelled microbubble ($R_{SF} = 2 \mu\text{m}$, $\mu_s = 45 \times 10^{-9} \text{ kg/s}$, $\chi = 9 \text{ N/m}$, $k_B = 2.25 \times 10^{-16} \text{ N m}$, $\delta = 15 \text{ nm}$) subject to (a)–(c) an initial prestress of $U_d = -0.004 \mu\text{m}$ and (d) no initial prestress and an acoustic disturbance of $f = 1.7 \text{ MHz}$; $R_{ps} \approx 0.999$, $\hat{B} \approx 6 \times 10^{-6}$, $\hat{R}e_s \approx 2$.

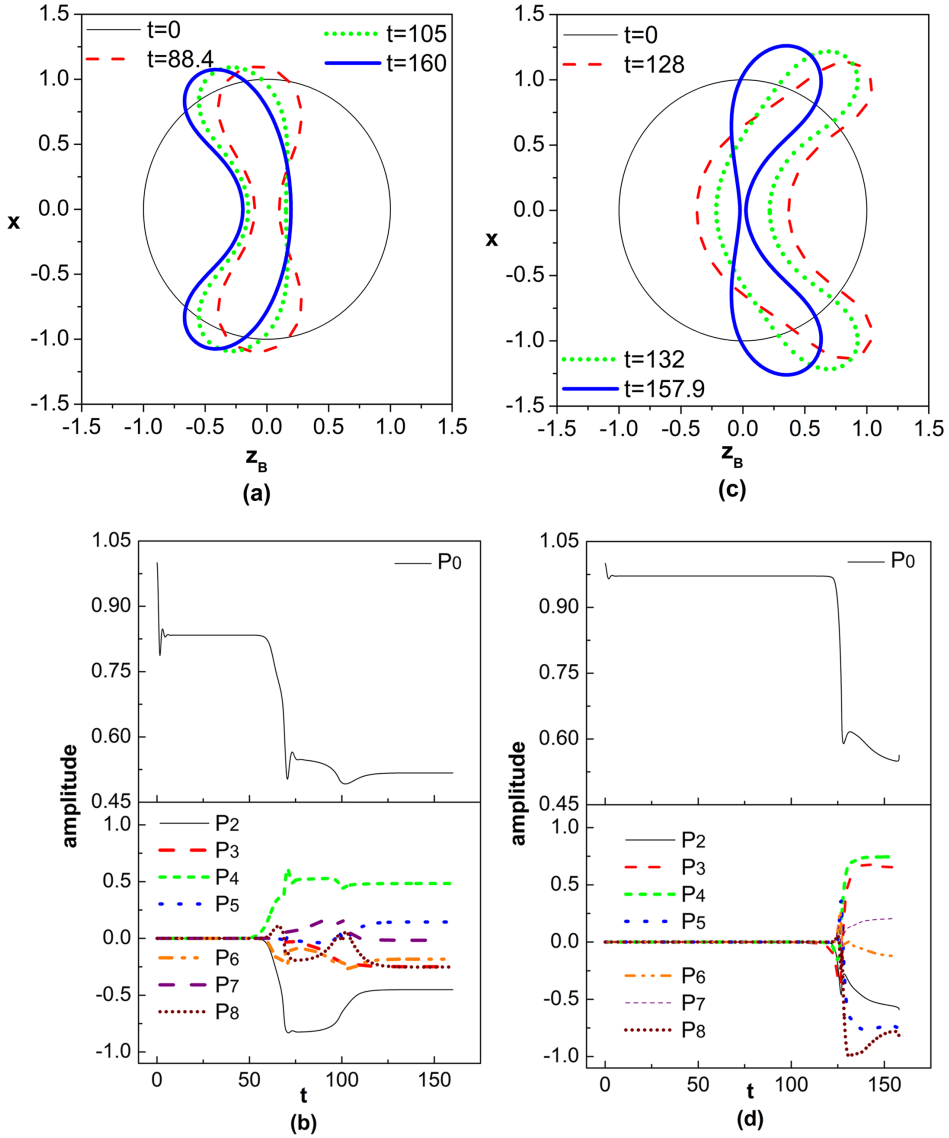


FIG. 10. Temporal evolution of bubble shape (a, c) and of the breathing, P_0 , and shape mode decomposition (b), (d) for a lipid-coated microbubble ($R_{SF} = 3.6 \mu\text{m}$, $\mu_s = 60 \times 10^{-9} \text{ kg/s}$, $\chi = 0.24 \text{ N/m}$, $k_B = 3 \times 10^{-14} \text{ N m}$, $\delta = 1 \text{ nm}$) in an unbounded flow environment. Simulations for a step change pressure disturbance and $\mu_{sh}/\mu_s = 1$, (a), (b) $\varepsilon = 2$ without prestress and (c), (d) $\varepsilon = 0.3$ with prestress with $U_d = -0.46 \mu\text{m}$ ($R_{ps} \approx 0.872$); $\hat{B} \approx 0.01$, $\hat{Re}_s \approx 8.3$.

amplitude $\varepsilon = 0.3$ is selected so that it leads to the same compressed spherical configuration with an amplitude $\varepsilon = 1.75$ on a stress-free shell. The buckled shapes are not the same for the above amplitudes but similar, dominated by the energetically favored P_2 and P_3 in the manner exhibited by Fig. 3. In this fashion buckled shapes are obtained at a significantly lower amplitude ε with respect to the stress-free state, in agreement with the bifurcation diagram and relevant shapes shown in Fig. 3(a). Note also that the final microbubble shape nearly exhibits contact at the end of the

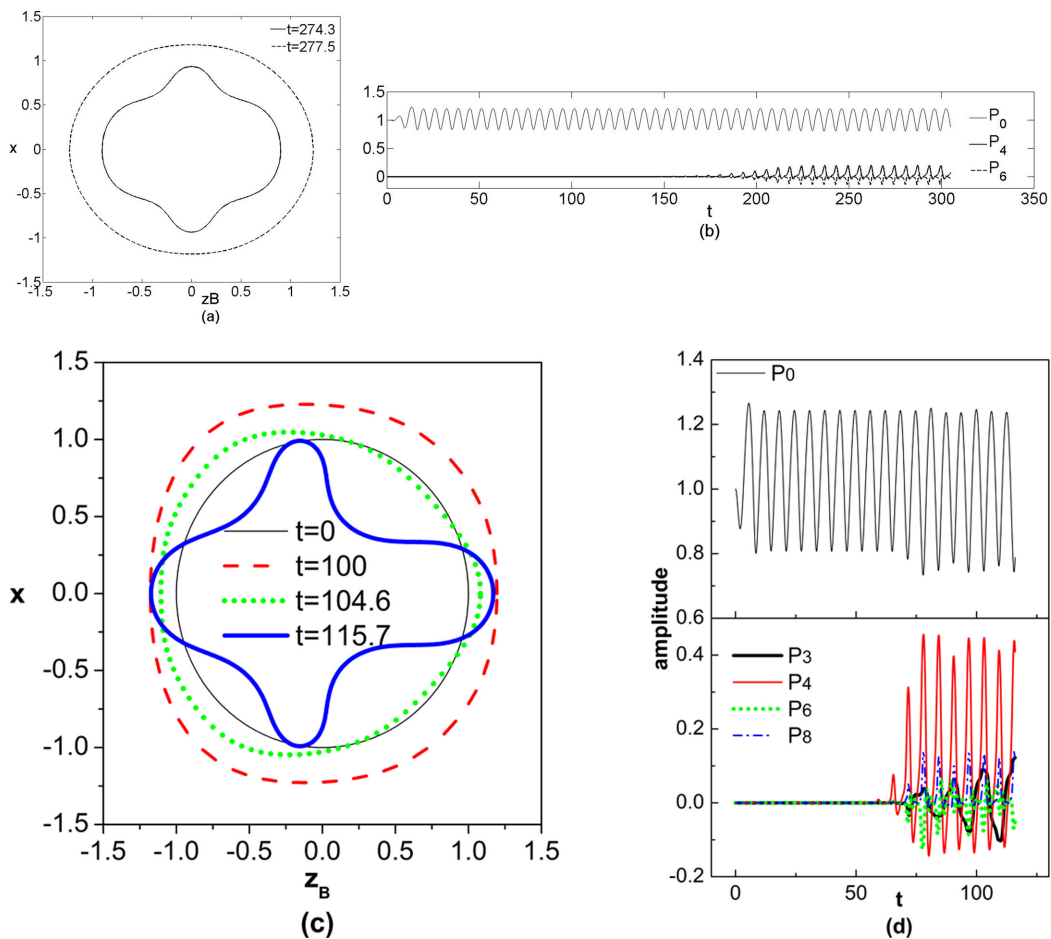


FIG. 11. Temporal evolution of bubble shape (a), (c) and of the breathing, P_0 , and shape mode decomposition (b), (d) for a lipid-coated microbubble ($R_{SF} = 3.6 \mu\text{m}$, $\mu_s = 60 \times 10^{-9} \text{ kg/s}$, $\chi = 0.24 \text{ N/m}$, $k_B = 3 \times 10^{-14} \text{ N m}$, $\delta = 1 \text{ nm}$) in an unbounded flow environment. Simulations without prestress for an acoustic pressure disturbance, with $f = 1.7 \text{ MHz}$ and (a), (b) $\varepsilon = 2$, for an inviscid liquid and $\mu_{sh}/\mu_s = 1$, and (c), (d) $\varepsilon = 2.1$ for liquid water and $\mu_{sh}/\mu_s = 0.05$; $R_{ps} = 1$, $\hat{B} \approx 0.01$, $\hat{Re}_s \approx 8.3$.

saturation as also indicated by the equivalent shapes in Fig. 3 for both asymmetric and symmetric shapes for this amplitude range.

The dynamic behavior of the same coated microbubble was examined subject to an acoustic disturbance by Tsigliffis and Pelekasis [26] and in an ensuing study by Vlachomitrou and Pelekasis [22,23] neglecting or accounting for viscous dissipation in the surrounding liquid, respectively. In both studies an initially stress-free state was considered while the dilatational and shear shell viscosities were taken to be the same. In the former study parametric instability was captured at an amplitude of $\varepsilon = 2$ and $\omega_f = 2\pi 1.7 \text{ MHz}$ while the microbubble was seen to perform saturated pulsations between the spherical shape at expansion and the buckled shape at compression dominated by the parametrically excited P_4 , Fig. 11(a). At the same time the time evolution of P_0 exhibits a type of “compression-only” response in the form of preferential excursion to compression as a result of energy transfer between P_0 and P_4 [Fig. 11(b)]. Taking water as the surrounding medium and using the stress-free radius and forcing frequency used in the above simulations as indicative

values we obtain the Reynolds number, $Re = \rho\omega_f R_{SF}^2/\mu \approx 138$, based on which we expect that liquid viscosity will not bear a dramatic effect on the dynamic response of the microbubble.

Indeed parametric excitation of P_4 is also captured by Vlachomitrou and Pelekasis [22,23]; however, the impact of liquid viscosity is that it decelerates the onset of deformation and energy transfer between P_0 and P_4 thus increasing the amplitude threshold to $\varepsilon = 2.5$ and nearly eliminating the “compression-only” response pattern. Nevertheless, the microbubble tends to pulsate around the buckled shape dominated by P_4 as can be gleaned by the emerging shapes and volume compression. This is in cross reference to the bifurcation diagram [25] and the phase diagram in Fig. 7(b) both obtained in the absence of prestress, indicating P_4 as the first emerging parametrically unstable shape mode. Upon introducing a distinctly reduced shear shell viscosity, dynamic simulations in the absence of prestress initially capture the well-documented radial excursion towards expansion during the phase of negative external overpressure, due to the strain-softening nature of the shell; see [3,26]. However, the microbubble eventually exhibits a more intense volume compression during the compressive phase of the pressure disturbance as illustrated in Figs. 11(c) and 11(d) when $\varepsilon = 2.1$. In the latter figures the shape and volume of the pulsating bubble are oscillating between the two extremes corresponding to a spherical shell during maximal expansion and the buckled shape dominated by P_4 at compression. Owing to the large number of unstable modes, as illustrated by the phase diagram of Fig. 7(b), the shape is polluted by P_3 during compression and the volume pulsation and growth of shape modes do not reach saturation. Instead they exhibit an oscillatory behavior due to simultaneous growth of P_4 and P_3 , Figs. 11(c) and 11(d).

1. Combined effect of prestress and reduction of shear viscosity

Motivated by the impact of shell viscosity on the emerging shape modes we proceed to study the effect of a certain discrepancy between the shear and dilatational viscosity of the shell. We perform a parametric study on the dynamic response of a microbubble with varying degree of such a discrepancy in favor of the dilatational viscosity, in order to facilitate energy transfer from the breathing to shape modes upon saturation of the pulsation. Indeed, decreasing the shear viscosity reduces the threshold for parametric shape mode excitation for cases with or without prestress. However, the absence of prestress does not induce any significant volume reduction during saturation except for cases with significant discrepancy between the shear and dilatational shell viscosity, as illustrated in Figs. 11(c) and 11(d) where the shape is dominated by P_4 and P_3 . On the contrary, coexistence of prestress with a reduction in the shear viscosity of the shell allows for the compression-only response pattern to clearly emerge for a relatively wide range of shell viscosities, as illustrated by the time evolution of shape modes discussed below.

To this end, we maintained the properties of the contrast agent employed in simulations shown in Fig. 11, while gradually reducing the shear viscosity of the shell down to $\mu_{sh}/\mu_s = 0.05$ with the dilatational one kept constant, $\mu_s = 60 \times 10^{-9}$ kg/s. We also set the initial compression of the bubble to $U_d = -0.46 \mu\text{m}$ and thus the initial radius of the bubble, $R_0 = 3.14 \mu\text{m}$, is slightly above the critical threshold for static buckling. In particular, it corresponds to a radial compression of $R_0/R_{SF} \approx 0.872$ when the critical compression for buckling to occur is $R_B/R_{SF} \approx 0.87$ pertaining to a bifurcating branch emerging at a critical amplitude $\varepsilon_{cr} \approx 0.04$ that is dominated by P_3 . The bifurcation diagram in Fig. 3(a) illustrates the evolution of the three major nonspherical bifurcating branches that exist for a microbubble with the above viscoelastic properties, dominated by an asymmetric, P_3 , and two symmetric shape modes, P_2 and P_4 , that emerge in the order cited in terms of amplitude. It provides a comprehensive bifurcation diagram in the $(V/V_0, \varepsilon)$ plane illustrating the structure of static equilibrium and the evolution of deformed shapes as a step change on the external overpressure is applied, on a coated microbubble that is prestressed as a result of gas leakage through the bubble shell.

In order to obtain a clearer picture of the selection process pertaining to the emerging deformed shapes, we examine graphs of the amplitude thresholds for the parametric excitation of specific Legendre modes for the cases with and without prestress in Figs. 7(a) and 7(b), respectively, and

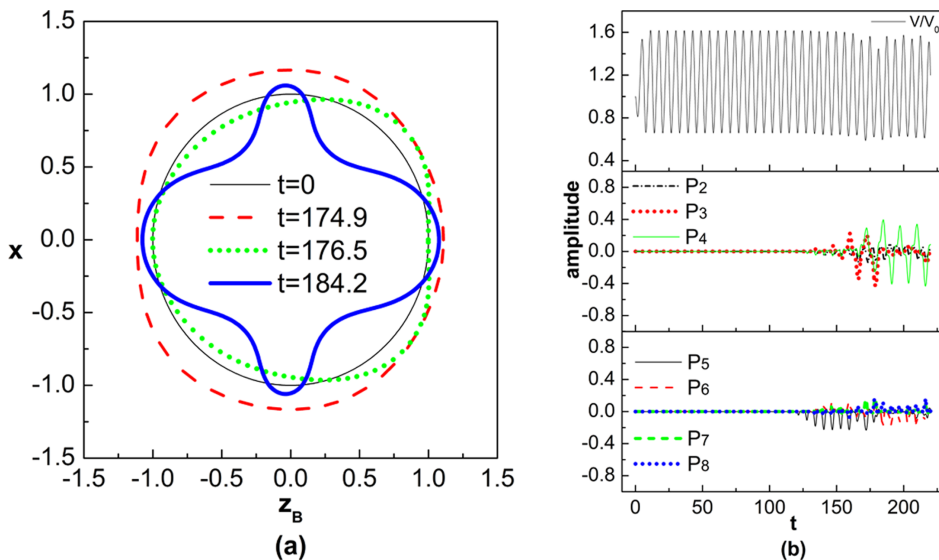


FIG. 12. Temporal evolution of bubble shape (a) and the volume and shape mode pulsation (b), for a lipid-coated microbubble ($R_{SF} = 3.6 \mu\text{m}$, $\mu_s = 60 \times 10^{-9} \text{ kg/s}$, $\chi = 0.24 \text{ N/m}$, $k_B = 3 \times 10^{-14} \text{ N m}$, $\delta = 1 \text{ nm}$) subject to an acoustic disturbance with $f = 1.7 \text{ MHz}$ in an unbounded flow environment for the case with prestress, $U_d = -0.46 \mu\text{m}$ ($R_{ps} \approx 0.872$), ratio $\mu_{sh}/\mu_s = 0.6$, and sound amplitude $\varepsilon = 1.3$; $k_B/((\chi R_0^2) \approx 0.01$; $\hat{B} \approx 0.01$, $\hat{R}e_s \approx 8.3$.

a forcing frequency of 1.7 MHz. In these phase diagrams the lines corresponding to amplitude thresholds for static buckling to occur, leading to the major bifurcating branches, are also shown along with the amplitude threshold for DB to occur within 10 cycles of the forcing. The latter is an upper threshold in the imposed sound amplitude beyond which loss of cohesion and shell destruction is expected to take place.

When the shear and dilatational viscosities are relatively large and equal in magnitude, growth of shape modes is suppressed for medium sound amplitudes. Due to the prestress of the shell, the threshold for static buckling to occur is well below that for parametric shape mode excitation. The latter, as predicted by our numerical simulations, is located slightly below the prediction of the phase diagram [Fig. 7(a)]. In the narrow gap between the threshold for parametric instability and DB, $1.8 \leq \varepsilon \leq 2.3$, a number of symmetric and asymmetric shape modes emerge that lead to a compression-only type response. However, the simulations eventually stop due to contact of different regions of the interface. This behavior is anticipated by the corresponding bifurcation diagram [Figs. 3(a)–3(c)], which predicts contact of the interface for shapes evolving along the symmetric and asymmetric branches in the above amplitude range.

Upon raising the discrepancy in favor of dilatational viscosity, i.e., setting $\mu_{sh}/\mu_s = 0.6$, growth of P_4 eventually dominates the shape of the bubble that oscillates between the nearly spherical shape at expansion and the P_4 -dominated shape at compression [Figs. 12(a) and 12(b)]. The final volume reduction is of the order predicted by the bifurcation diagram of the P_4 branch [Figs. 3(a) and 3(d)] for the same amplitude. P_4 is also the mode identified by parametric stability [Fig. 7(a)] as the one that is first excited for this parameter range.

Further reduction of shell shear viscosity to $\mu_{sh}/\mu_s = 0.3$ facilitates growth of P_2 via parametric instability, as registered in the respective phase diagram in Fig. 7(a). This reflects in the acquired shapes and the additional volume reduction during compression; see also Figs. 13(a) and 13(b). The bubble acquires shapes that essentially belong to the branch characterized by oblate P_2 shapes, as it bypasses the prolate part of this branch due to its larger energy content, and tends to produce

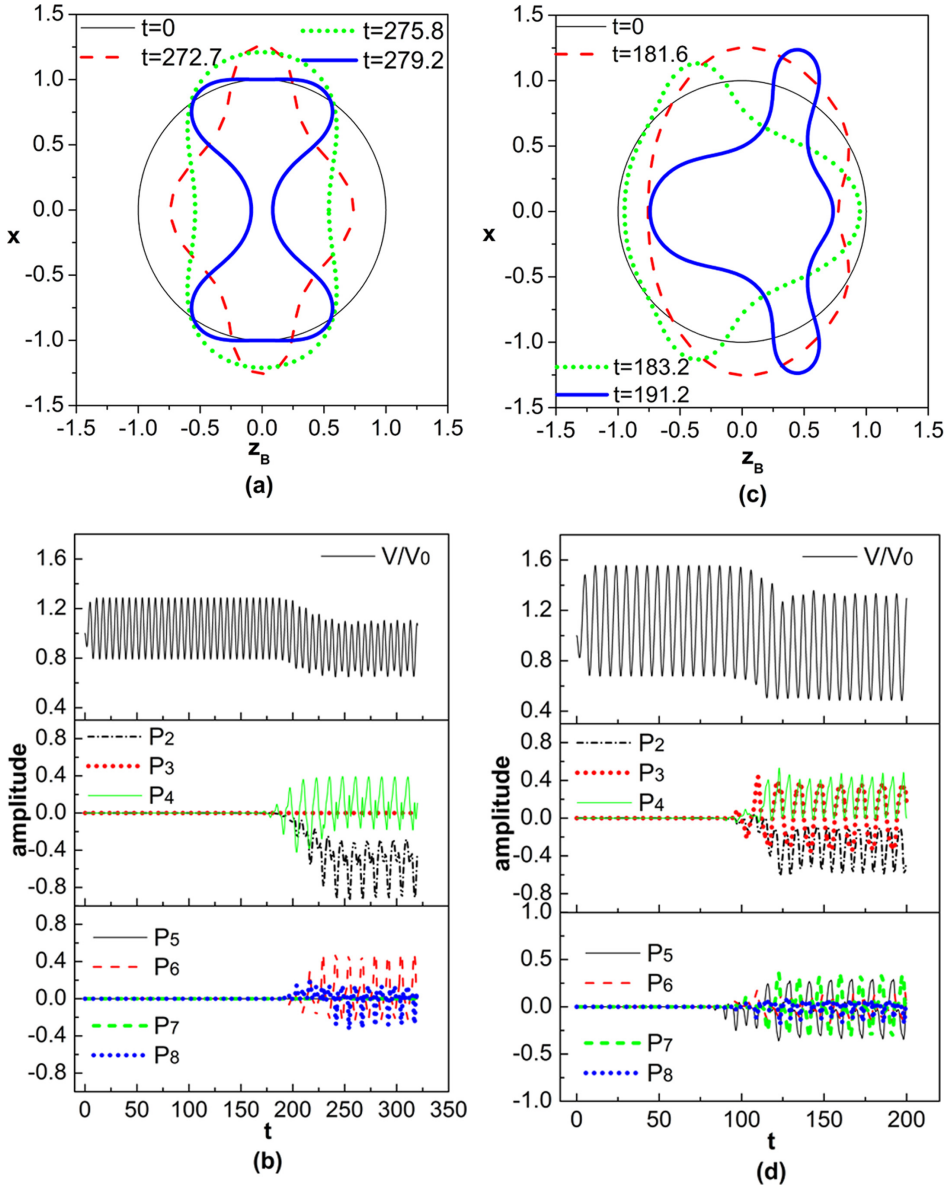


FIG. 13. Temporal evolution of bubble shape (a), (c) and the volume and shape mode pulsation (b), (d), for a lipid-coated microbubble ($R_{SF} = 3.6 \mu\text{m}$, $\mu_s = 60 \times 10^{-9} \text{ kg/s}$, $\chi = 0.24 \text{ N/m}$, $k_B = 3 \times 10^{-14} \text{ N m}$, $\delta = 1 \text{ nm}$) subject to an acoustic disturbance with $f = 1.7 \text{ MHz}$ in an unbounded flow environment for the case with prestress, $U_d = -0.46 \mu\text{m}$ ($R_{ps} = 0.872$), and $\mu_{sh}/\mu_s = 0.3$ when (a), (b) $\varepsilon = 0.7$ and (c), (d) $\varepsilon = 1.2$; $k_B/(\chi R_0^2) \approx 0.01$; $\hat{B} \approx 0.01$, $\hat{R}e_s \approx 8.3$.

the energetically preferred oblate shapes. In fact, due to the finite forcing period the microbubble does not have the time to acquire the shape captured by static analysis in Fig. 3(c), corresponding to an amplitude of 0.7, which exhibits contact. Rather it pulsates around oblate shapes with varying degree of deformation depending on the extent of P_4 growth that is also parametrically triggered at this parameter range. Increasing the sound amplitude to 1.3 parametrically excites P_3 along with P_2 on a much faster timescale [Fig. 7(a)], and the dynamic response is characterized by hybrid shapes

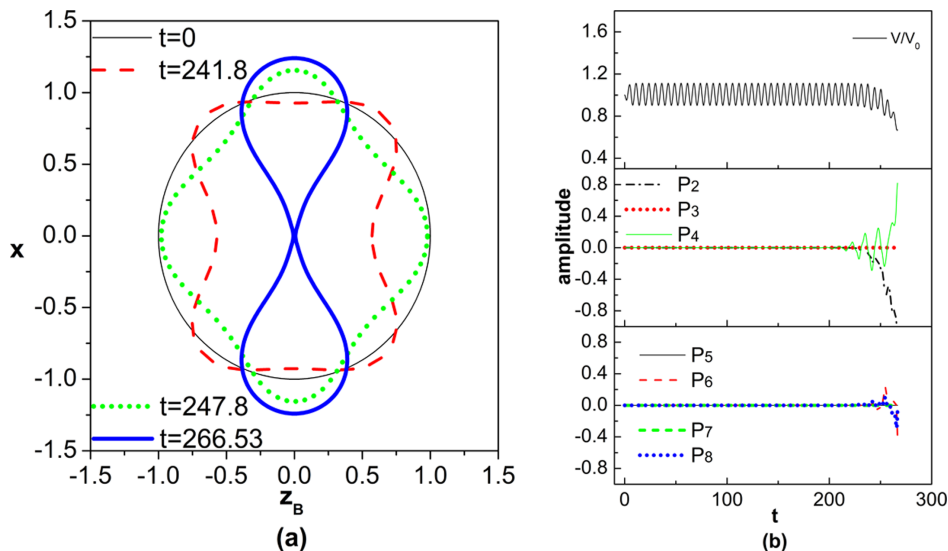


FIG. 14. Temporal evolution of bubble shape (a) and the volume and shape mode pulsation (b), for a lipid-coated microbubble ($R_{SF} = 3.6 \mu\text{m}$, $\mu_s = 60 \times 10^{-9} \text{ kg/s}$, $\chi = 0.24 \text{ N/m}$, $k_B = 3 \times 10^{-14} \text{ N m}$, $\delta = 1 \text{ nm}$) subject to an acoustic disturbance with $f = 1.7 \text{ MHz}$ in an unbounded flow environment for the case with prestress, $U_d = -0.46 \mu\text{m}$ ($R_{ps} = 0.872$), and $\mu_{sh}/\mu_s = 0.05$, $\varepsilon = 0.3$; $\hat{B} \approx 0.01$, $\hat{R}e_s \approx 8.3$.

dominated by oblate P_2 and P_3 while achieving even stronger volume compression [Figs. 13(c) and 13(d)]. It is as if the microbubble pulsates along the oblate P_2 branch [Figs. 3(a) and 3(c)] with varying levels of deformation involving the asymmetric P_3 mode, and a stronger excursion towards compression in comparison with the expansion phase of its pulsation, with reference to the initial spherical configuration. Clearly, for this parameter range, the tendency to compress as they deform overwhelms the standard tendency of spherical strain-softening shells to expand, and this is the kind of response pattern registered in the literature as compression only.

By imposing an acoustic disturbance of amplitude 0.3 on a microbubble with an even lower shear shell viscosity $\mu_{sh}/\mu_s = 0.05$, the compression-only effect is again captured dominated by oblate P_2 shapes. In fact, it is so intense that after its onset the bubble tends to remain constantly in the compressed phase compared to the initial configuration. Furthermore, it is of great interest that, as illustrated by Figs. 14(a) and 14(b), the shape and volume the bubble acquires during maximum compression are very close to the static solution corresponding to an imposed amplitude of 0.3 [Figs. 3(a) and 3(c)] exhibiting contact between the two poles at the equatorial plane. This is a result of the nearly negligible shear shell viscosity that allows for quick growth of shape modes that periodically lead the dynamics towards the preferred static configuration. A slight increase of the shear shell viscosity to $\mu_{sh}/\mu_s = 0.1$ or raising the forcing frequency to $f = 2 \text{ MHz}$ prevent contact from taking place during the compression phase of the bubble pulsation by damping parametric growth of shape modes or, equivalently, decreasing the duration of the excitation process during compression; see Fig. 15. In fact, when the forcing frequency is raised [Figs. 15(c) and 15(d)], the bubble eventually exhibits saturated pulsations around the asymmetric P_3 mode that is also preferentially excited at this amplitude and shear shell viscosity range [Fig. 7(a)] and is energetically favored in the bifurcation diagram [Figs. 3(a) and 3(b)] based on static analysis.

2. Effect of shell elasticity

In this subsection we proceed to examine how shell elasticity affects the onset of the compression-only behavior. We consider two shells obeying a strain-softening constitutive law,

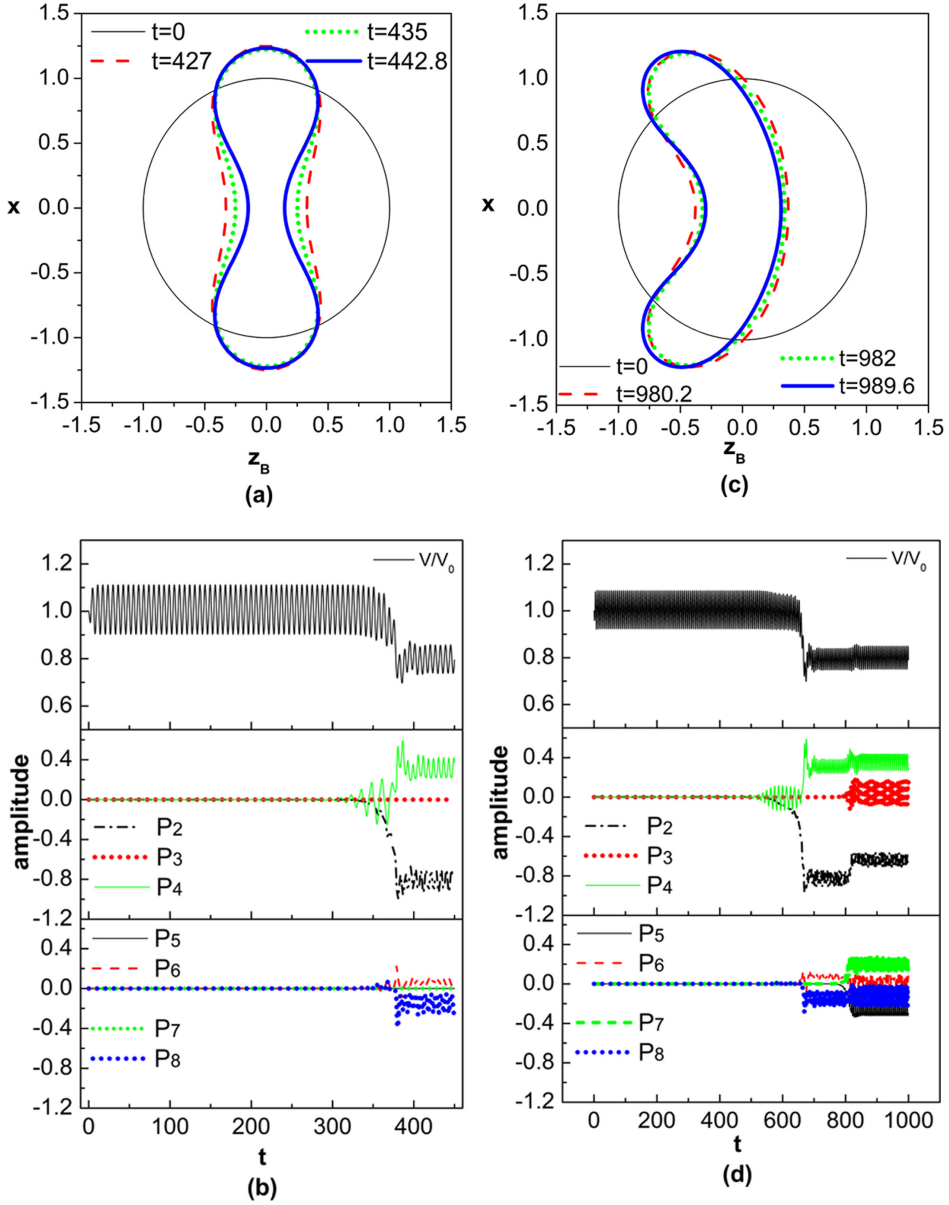


FIG. 15. Temporal evolution in an unbounded flow environment of bubble shape (a), (c) and volume and shape mode pulsation (b), (d), for a lipid-coated microbubble ($R_{SF} = 3.6 \mu\text{m}$, $\mu_s = 60 \times 10^{-9} \text{ kg/s}$, $\chi = 0.24 \text{ N/m}$, $k_B = 3 \times 10^{-14} \text{ N m}$, $\delta = 1 \text{ nm}$) with prestress, $U_d = -0.46 \mu\text{m}$ ($R_{ps} = 0.872$), subject to an acoustic disturbance with amplitude $\varepsilon = 0.3$ and (a), (b) $f = 1.7 \text{ MHz}$, $\mu_{sh}/\mu_s = 0.1$, $\hat{B} \approx 0.01$, $\hat{R}e_s \approx 8.3$ and (c), (d) $f = 2 \text{ MHz}$, $\mu_{sh}/\mu_s = 0.05$, $\hat{B} \approx 0.01$, $\hat{R}e_s \approx 9$, 8.

namely a softer and a harder shell compared to the one studied in Sec. VB1 in terms of area dilatation modulus, $\chi = 0.12 \text{ N/m}$ and $\chi = 0.48 \text{ N/m}$. It is a parametric study which, along with the case with a polymeric shell, focuses on the impact of a progressively harder shell on the compression-only effect by gradually raising the ratio between bending and membrane stiffness, $k_B/(\chi R_0^2)$. The shell with $\chi = 0.12 \text{ N/m}$ is a soft shell and consequently it is not as conducive

to significant bending and requires larger amplitudes for buckling to take place. The bifurcation diagram for this shell [Fig. 2(a)] is similar to the case with $\chi = 0.24$ N/m, with the exception of the P_3 branch that evolves towards prolate rather oblate shapes along with the P_4 branch. Its dynamic response subject to an acoustic disturbance with forcing frequency $\omega_f = 2\pi 1.7$ MHz, under a certain amount of prestress, $R_{SF} = 3.6 \mu\text{m}$, $U_d = -0.61 \mu\text{m}$, does not leave a useful amplitude window for sufficient growth of shape modes. As a result deformation and static buckling take place above the threshold for DB, particularly for small differences between shell dilatation and shear viscosity; see also Fig. 6. As the shear shell viscosity decreases, $\mu_{sh}/\mu_s \leq 0.65$, shape modes corresponding to the major bifurcation branches become parametrically unstable and provide the excursion to smaller volumes during compression typically associated with the compression-only type response pattern. Based also on the phase diagram provided in Fig. 6 and the corresponding bifurcation diagram in Fig. 2(a) for $\chi = 0.12$ N/m, P_3 and P_4 become unstable leading to a pulsation between the spherical configuration at maximum expansion and prolate shapes that are asymmetric and exhibit significant volume reduction with varying amount of P_4 at maximum compression; see also Figs. 2(c) and 2(d). Figures 16 and 17 illustrate this type of behavior for the above parameter range and is evident that as shear viscosity is further reduced compression-only behavior is captured at lower sound amplitudes. It should be noted that the microbubble never settles to a pulsation around the extreme oblate shapes observed for simulations with a larger area dilatation modulus shown in Figs. 12–15, despite the fact that P_2 also grows parametrically especially for very small shear viscosities. This is attributed to the fact that oblate P_2 shapes, which are preferred based on their total energy at static equilibrium, exhibit significant distortion and bending in comparison with the prolate ones dominated by P_3 and P_4 , and this is not favored in the dynamic response of the soft shell studied in Figs. 16 and 17.

The case of a shell with area dilatation modulus $\chi = 0.48$ N/m is similar to the case with $\chi = 0.24$ N/m studied in Sec. VB 1. This pertains both to their respective bifurcation diagrams, Figs. 3(a) and 4(a), which are both dominated by the P_2 and P_3 branches with their oblate parts exhibiting significant volume compression, but also to their respective phase diagrams [Figs. 7(a) and 8]. The latter graphs exhibit progressive acceleration of parametric excitation of shape modes P_2 , P_3 , and P_4 , in terms of lowering the amplitude thresholds, as the shear shell viscosity decreases. Thus, the above modes tend to dominate the dynamic response in the amplitude window defined by the static and DB thresholds. This gives rise to bubble pulsations in the neighborhood of the P_2 and P_3 branches [Figs. 4(b) and 4(c)], especially at maximum compression. Figure 18 illustrates this pattern as the shear viscosity of the shell decreases. In this case the bubble tends to achieve saturated pulsation of the shape modes around a compressed volume, that decreases approaching the equivalent static configuration along the oblate P_2 or P_3 branch. The former shapes also contain P_4 to a large extent as they entail gradual approach and eventually contact of the opposite poles in the equator region. The obtained shapes reflect this aspect since growth of P_4 is facilitated by parametric mode excitation. They also exhibit varying levels of P_3 contamination as the corresponding branch occurs for the same parameter range as the oblate P_2 one. In fact, for the cases shown in Figs. 18(c), 18(d), 19(a), and 19(b) obtained for the same sound amplitude but different shear viscosities, the simulation for the smaller ratio of shell viscosities, $\mu_{sh}/\mu_s = 0.05$, triggers faster growth of P_3 that leads to asymmetric contact of the opposite pole regions. Increasing the forcing frequency to 2.5 MHz bears the same effect on the bubble dynamics with raising the shear viscosity; compare differences between Figs. 19(a) and 19(b) and 19(c) and 19(d) against those between Figs. 18(c) and 18(d) and 18(a) and 18(b). It decelerates growth of shape modes and allows for saturated pulsations [Figs. 19(c) and 19(d)]. Consequently, a compression-only type pattern is established that is dominated by the asymmetric P_5 and P_3 modes along with a certain amount of P_4 .

It should be stressed that even though growth of P_4 and P_5 is also predicted by the phase diagram obtained when $\chi = 0.48$ N/m (Fig. 8), and there are distinct branches dominated by the prolate P_4 and P_5 in the corresponding bifurcation diagram, such shapes were captured but did not dominate the simulations. This is due to the fact that the respective branches do not evolve in the amplitude range for which parametric mode excitation of prolate P_4 or P_5 is possible; see also the

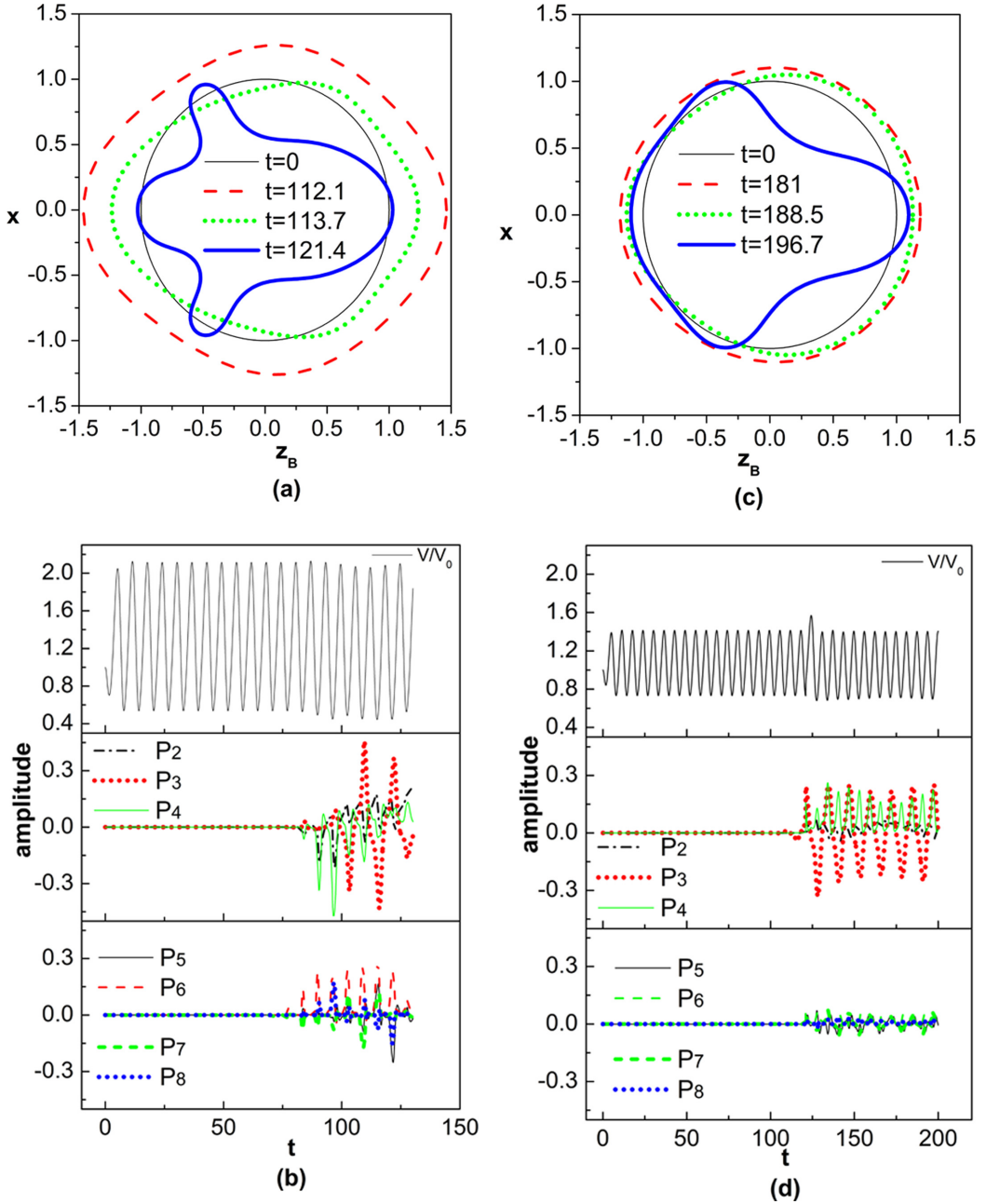


FIG. 16. Temporal evolution of bubble shape (a), (c) and the volume and shape mode pulsation (b), (d), for a lipid-coated microbubble ($R_{SF} = 3.6 \mu\text{m}$, $\mu_s = 60 \times 10^{-9} \text{ kg/s}$, $\chi = 0.12 \text{ N/m}$, $k_B = 3 \times 10^{-14} \text{ N m}$, $\delta = 1 \text{ nm}$) subject to an acoustic disturbance with $f = 1.7 \text{ MHz}$ in an unbounded flow environment for the case with prestress, $U_d = -0.61 \mu\text{m}$ ($R_{ps} = 0.83$), and (a), (b) $\mu_{sh}/\mu_s = 0.65$, $\varepsilon = 2.1$ and (c), (d) $\mu_{sh}/\mu_s = 0.15$, $\varepsilon = 1$; $\hat{B} \approx 0.02$, $\hat{Re}_s \approx 8.3$.

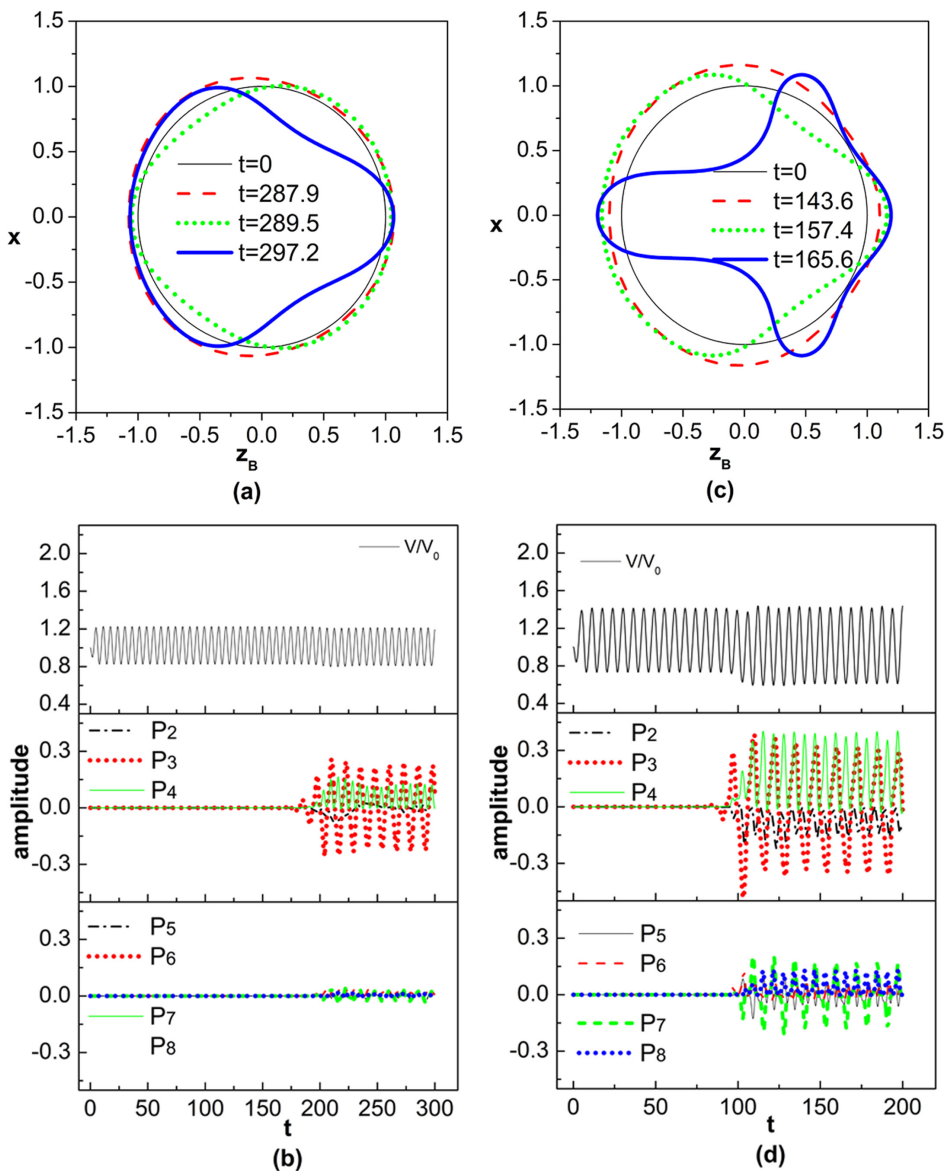


FIG. 17. Temporal evolution of bubble shape (a), (c) and of the volume and shape mode pulsation (b), (d), for a lipid-coated microbubble ($R_{SF} = 3.6 \mu\text{m}$, $\mu_s = 60 \times 10^{-9} \text{ kg/s}$, $\chi = 0.12 \text{ N/m}$, $k_B = 3 \times 10^{-14} \text{ N m}$, $\delta = 1 \text{ nm}$) subject to an acoustic disturbance with $f = 1.7 \text{ MHz}$ in an unbounded flow environment for the case with prestress, $U_d = -0.61 \mu\text{m}$ ($R_{ps} = 0.83$), and (a), (b) $\mu_{sh}/\mu_s = 0.05$, $\varepsilon = 0.6$ and (c), (d) $\mu_{sh}/\mu_s = 0.05$, $\varepsilon = 0.8$; $\hat{B} \approx 0.02$, $\hat{R}e_s \approx 8.3$.

bifurcation diagram in Fig. 4(a) in cross-reference with the phase diagram for such shells provided in Fig. 8.

3. The case of polymeric shells

Our simulations have thus far demonstrated that shell rheology plays a key role in triggering the onset of the compression-only effect. However, such a response pattern has not been reported

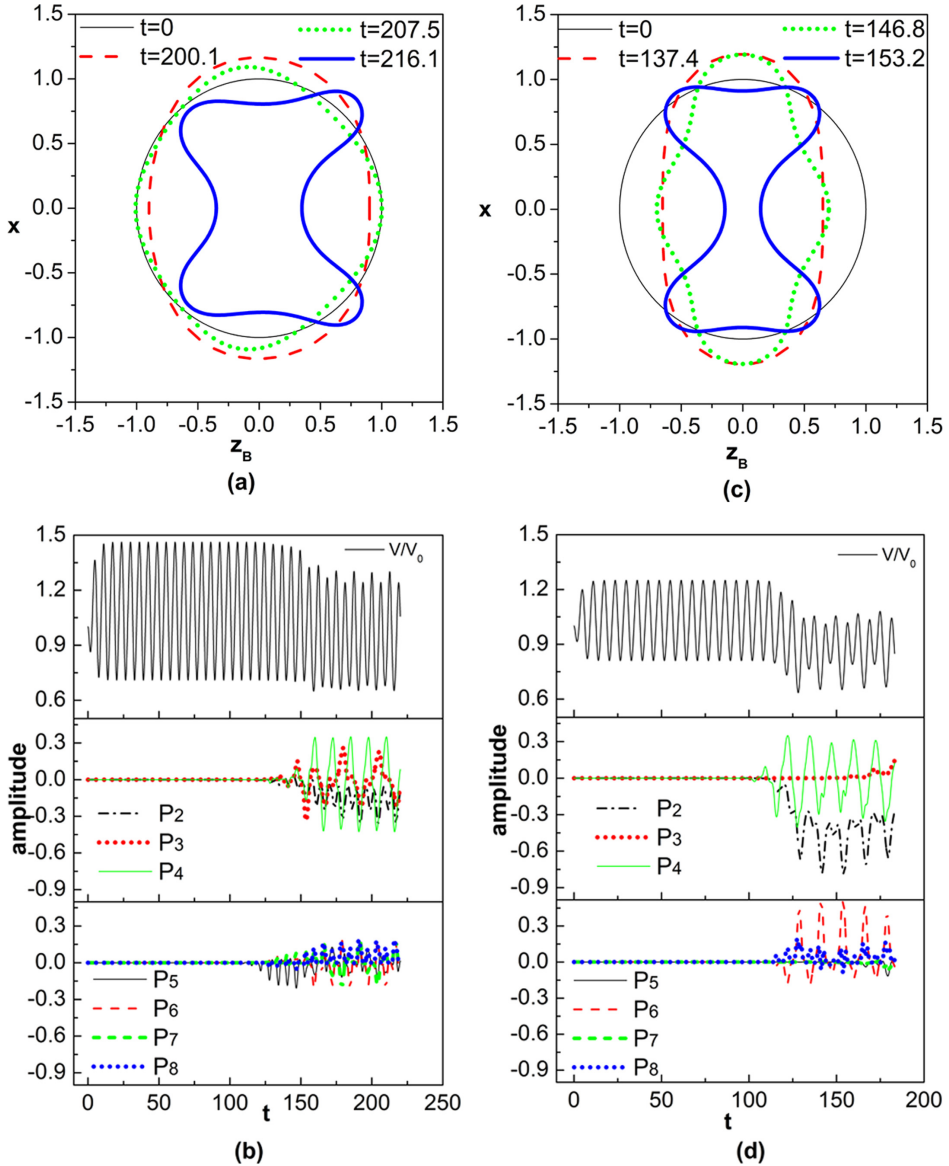


FIG. 18. Temporal evolution of bubble shape (a), (c) and of the volume and shape mode pulsation (b), (d), for a lipid-coated microbubble ($R_{SF} = 3.6 \mu\text{m}$, $\mu_s = 60 \times 10^{-9} \text{ kg/s}$, $\chi = 0.48 \text{ N/m}$, $k_B = 3 \times 10^{-14} \text{ N m}$, $\delta = 1 \text{ nm}$) subject to an acoustic disturbance in an unbounded flow environment for the case with prestress, $U_d = -0.3 \mu\text{m}$ ($R_{ps} = 0.916$), and forcing frequency $f = 1.7 \text{ MHz}$ with (a), (b) $\mu_{sh}/\mu_s = 0.65$, $\varepsilon = 1$ and (c), (d) $\mu_{sh}/\mu_s = 0.2$, $\varepsilon = 0.6$; $\hat{B} \approx 0.05$, $\hat{R}e_s \approx 8.3$.

in experimental studies involving polymer-shelled microbubbles. In an effort to investigate the behavior of this type of shells we consider the PB-127 microbubble that occupies a polymer shell with a stress-free radius of $R_{SF} = 2 \mu\text{m}$ and $\delta = 15 \text{ nm}$ thickness, an area dilatation modulus $\chi = 9 \text{ N/m}$ and a bending modulus equal to $k_B = 2.25 \times 10^{-16} \text{ N m}$. The dilatational and shear shell viscosities are initially set to $45 \times 10^{-9} \text{ kg/s}$. In the absence of prestress the phase diagram as a function of the ratio shell viscosity μ_{sh}/μ_s and sound amplitude shown in Fig. 9(c) for an acoustic

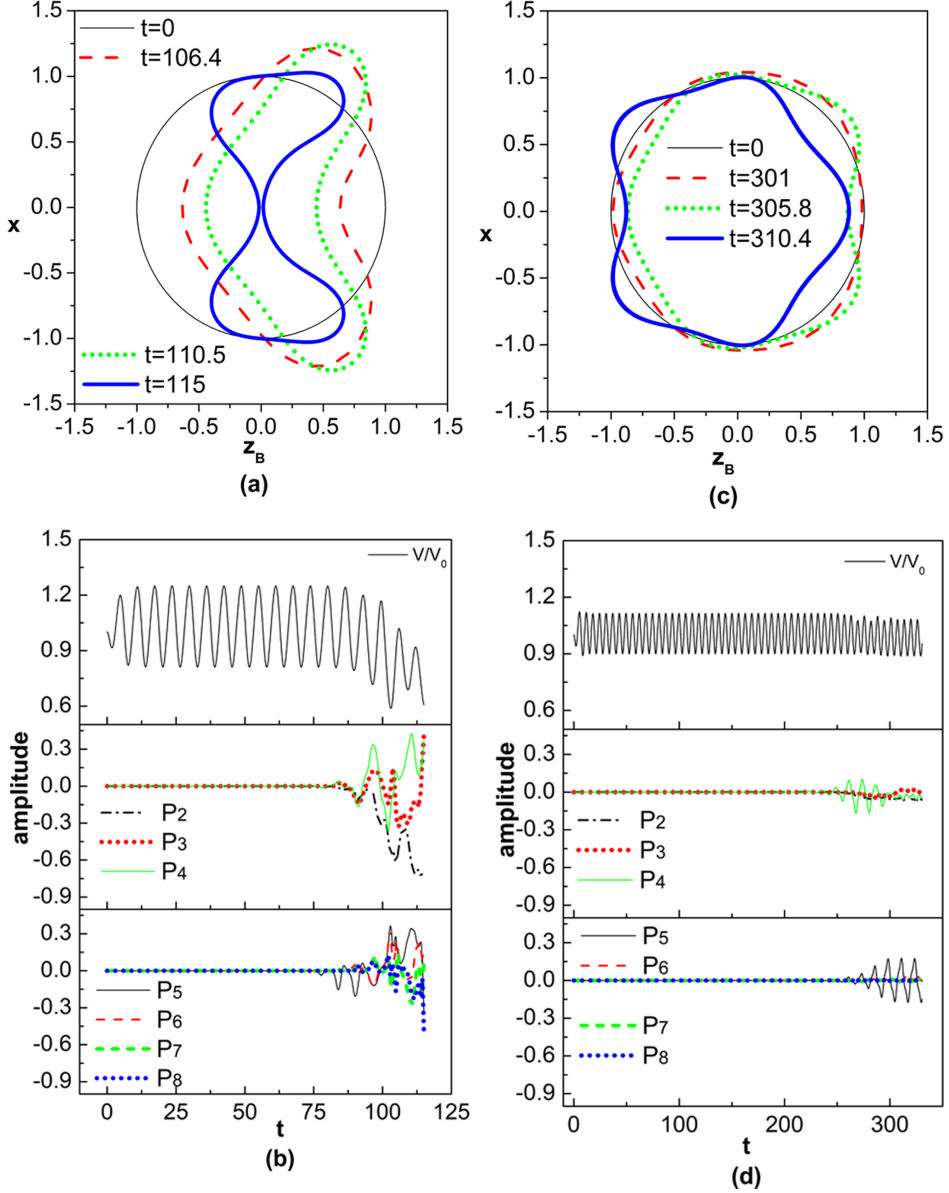


FIG. 19. Temporal evolution of bubble shape (a), (c) and the volume and shape mode pulsation (b), (d), for a lipid-coated microbubble ($R_{SF} = 3.6 \mu\text{m}$, $\mu_s = 60 \times 10^{-9} \text{ kg/s}$, $\chi = 0.48 \text{ N/m}$, $k_B = 3 \times 10^{-14} \text{ N m}$, $\delta = 1 \text{ nm}$) subject to an acoustic disturbance in an unbounded flow environment for the case with prestress, $U_d = -0.3 \mu\text{m}$ ($R_{ps} = 0.916$), and (a), (b) $\mu_{sh}/\mu_s = 0.05$, $f = 1.7 \text{ MHz}$, $\varepsilon = 0.6$, $\hat{R}e_s \approx 8.3$ and (c), (d) $\mu_{sh}/\mu_s = 0.05$, $f = 2.5 \text{ MHz}$, $\varepsilon = 0.6$, $\hat{R}e_s \approx 12.2$; $\hat{B} \approx 0.05$.

frequency of 1.7 MHz, contrary to the cases of lipid shells presented so far with a similar range of Re_s and Re_{sh} numbers, reveals that the DB limit lies below the static buckling threshold of the major bifurcating branches obtained for a stress-free initial condition; the bifurcating asymmetric and symmetric branches are dominated by P_{19} and P_{20} , respectively. In fact, it nearly coincides with the parametric mode excitation thresholds for some high modes (P_{19} and higher). As a result,

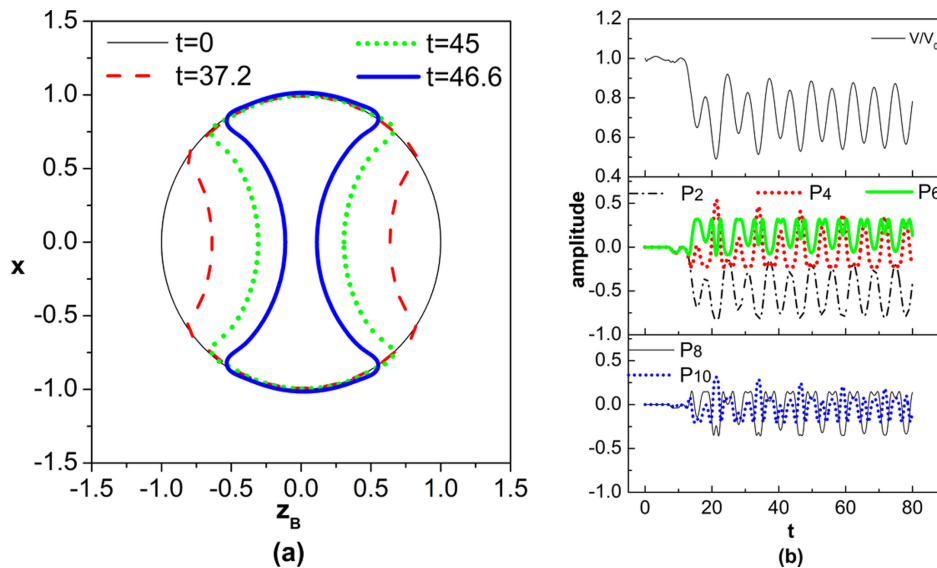


FIG. 20. Temporal evolution of bubble shape (a) and the volume and shape mode pulsation (b), for a PB-127 polymer-shelled contrast agent ($R_{SF} = 2 \mu\text{m}$, $\mu_s = 45 \times 10^{-9} \text{ kg/s}$, $\chi = 9 \text{ N/m}$, $k_B = 2.25 \times 10^{-16} \text{ N m}$, $\delta = 15 \text{ nm}$) in an unbounded flow environment for the case of $\mu_{sh}/\mu_s = 0.2$ with prestress, $U_d = -0.004 \mu\text{m}$ ($R_{ps} \approx 0.999$), subject to an acoustic disturbance with $f = 1.7 \text{ MHz}$ and amplitude $\varepsilon = 0.6$; $\hat{B} \approx 6 \times 10^{-6}$, $\hat{Re}_s \approx 2$.

even small sound amplitudes will lead to bubble collapse via rapid shell destabilization, and this is verified by our simulations.

When an initial prestress is introduced, the threshold for static buckling (Fig. 5) is considerably lower than the one of lipid shells and consequently the bubble can endure only very small levels of initial prestress. Nevertheless, even a small initial prestress, $U_d = -0.004 \mu\text{m}$, is sufficient to move the static buckling threshold in the phase diagram [Figs. 9(a) and 9(b)] below the DB threshold and the parametric shape mode limits, as was also reported in the case of lipid microbubbles. However, in this case the threshold in sound amplitude pertaining to parametric shape mode excitation lies on the upper boundary of the interval between the static and DB limits. In addition, several parametrically excited modes exist for the same amplitude range. Consequently, it is difficult for the shape mode that leads to a certain bifurcating branch to dominate the dynamics and give rise to the compression-only effect. The parametric study that we carried out for prestressed polymeric shells of the above type did not produce significant growth of shape modes below the DB limit and captured shell breakup above this threshold. Compression-only-type behavior was only captured in the case depicted in Fig. 20 for a considerable discrepancy between the shear and dilatational shell viscosity and a sound amplitude beyond the DB threshold, possibly owing to the damping effect of liquid viscosity. Growth of P_{20} is captured in the manner that is consistent with the bifurcation diagram, Fig. 5(c), in terms of the shape and volume at maximum compression for the same amount of prestress and sound amplitude.

VI. CONCLUSIONS

We carried out a theoretical/numerical study of freely pulsating coated microbubbles subject to an acoustic disturbance in order to capture the response pattern that is identified in the literature as compression-only behavior. It is a counterintuitive response since, especially strain-softening shells such as lipid monolayers, exhibit preferential excursion from equilibrium during expansion as a

result of the decrease in their area concentration of surfactant. It was thus found that compression only is associated with the onset of significantly compressed shapes that pulsate in the vicinity of static branches that bifurcate from the spherically symmetric configuration and are characterized by buckled shapes. Such shapes are energetically favored over spherical shapes based on static analysis, but their growth is relatively slow when it occurs spontaneously.

This process may be accelerated upon application of an acoustic disturbance in which case an initial prestress generates a window of sound amplitudes between the static buckling and the DB thresholds, within which parametric shape mode excitation is possible. We also provide phase diagrams outlining the parametric stability thresholds for lipid and polymeric shells corroborating the above pattern. This effect is more pronounced when there is significant discrepancy between the dilatational and shear viscosities of the shell in favor of the former. Growth of shape modes that lead to buckled shapes with significant volume compression and characterize the above static branches was thus captured.

It was seen that shells with a small shear viscosity facilitate energy exchange with the breathing mode leading to volume compression but also provide a distinctly lower amplitude threshold for the shape modes, mainly P_2 , P_3 , and P_4 , that steer the dynamics towards the buckled shapes. When the dilatation and shear viscosities are both large the amplitude threshold for parametric shape mode is large and close to the DB threshold. In this case, even in the narrow interval between them the large number of unstable modes does not allow for the static buckling configuration to be approached and the compression-only behavior is prevented. In fact, this is the case with the much harder polymeric shells which are characterized by a similar shell Reynolds, $\hat{Re}_s = \rho\omega_f R_{SF}^3/\mu_s$, but much smaller relative bending resistance, $\hat{B} = k_B/(\chi R_{SF}^2)$, in comparison with the lipid shells. For the former type shells the threshold for parametric mode excitation nearly coincides with that for DB to take place, even in the presence of prestress and a discrepancy between dilatational and shear viscosities, and consequently compression-only behavior is very rare. On the contrary lipid shells are more amenable to surface treatment that leads to varying viscoelastic properties which, in conjunction with a certain amount of prestress, may give rise to compression-only behavior via selective parametric shape mode excitation. Among lipid shells those with larger membrane elasticity, lower \hat{B} , are more conducive to buckling and are more likely to exhibit compression-only behavior. Simulations performed in the present study involving freely pulsating microbubbles, corroborate this pattern and capture the onset of dynamic response whereby the bubble pulsates mainly under compression with respect to the initial spherically symmetric configuration.

It is thus evident that understanding surface rheology is critical for the determination of the acoustic response of coated microbubbles, provides insight for the optimization of acoustic characterization of shell viscoelastic properties and can be a useful tool for the design of future contrast agents. In a future study we will present simulations of wall bounded microbubbles in response to acoustic disturbances and capture the combined impact of prestress and shear shell viscosity on the onset of compression-only behavior, the establishment of trapped pulsation in the vicinity of the wall vs bubble migration away from it, and the resulting enrichment of the available phase diagrams. In this fashion, it will also be possible by cross referencing phase diagrams produced by simulations with acoustic measurements that exhibit compression-only behavior, to obtain reliable estimates of shell properties including discrepancies between the two shell viscosities.

ACKNOWLEDGMENTS

This research has been carried out within the framework of the invitation ‘‘Expression of interest for holders of doctoral diploma, for scholarship for postdoctoral research’’ of the University of Thessaly, which is implemented by the University of Thessaly and is funded by the Stavros Niarchos Foundation. We also acknowledge financial support at the early stages of this work by the operational program ‘‘Education and lifelong learning-Aristeia I’’ entitled CONTAGEUSNUMSTADY, which was cofounded by the European Union (European Social Fund) and Greek national resources.

APPENDIX: $O(\hat{\varepsilon})$ CORRECTION TO THE TANGENTIAL STRESS COMPONENT

When treating separately the two shell viscosities the analysis presented in Sec. **III B** is only affected through the viscoelastic force of the shell introduced through the terms ΔF_n^0 , ΔF_n^1 , ΔF_t^1 . However, since only the dilatational shell viscosity contributes to the normal force balance equation, the terms ΔF_n^0 , ΔF_n^1 remain the same as in [15]. Regarding the tangential component ΔF_t^1 it is affected from both shell viscosities. The latter component reads as

$$\Delta F_t^1 = \left[-\frac{\partial \tau_{ss}^v}{\partial s} - \frac{1}{r_o} \frac{\partial r_o}{\partial s} (\tau_{ss}^v - \tau_{\varphi\varphi}^v) - \frac{\partial \tau_{ss}^{el}}{\partial s} - \frac{1}{r_o} \frac{\partial r_o}{\partial s} (\tau_{ss}^{el} - \tau_{\varphi\varphi}^{el}) - k_s q \right]^1. \quad (\text{A1})$$

The elastic stresses are not affected in this context, whereas viscous stresses are given by Eq. (11). In the framework of linear stability analysis λ_s , λ_ϕ are given by

$$\lambda_s = \hat{R} + \hat{\varepsilon}(w + u_\theta), \quad \lambda_\phi = \hat{R} + \hat{\varepsilon}(w + u \cot \theta_0), \quad (\text{A2})$$

with $\hat{\varepsilon}$ signifying the amplitude of the linear disturbance in the bubble shape. Upon introducing Eq. (A2) to Eq. (11) the viscous stresses are calculated:

$$\begin{aligned} \tau_{ss}^v = & \frac{2}{\hat{R}e_s} \frac{\dot{\hat{R}}}{\hat{R}} + \hat{\varepsilon} \left\{ \left(\frac{1}{\hat{R}e_s} + \frac{1}{\hat{R}e_{sh}} \right) \left[\frac{\dot{w} + \dot{u}_\theta}{\hat{R}} - \frac{\dot{\hat{R}}}{\hat{R}^2} (w + u_\theta) \right] \right. \\ & \left. + \left(\frac{1}{\hat{R}e_s} - \frac{1}{\hat{R}e_{sh}} \right) \left[\frac{\dot{w} + \dot{u} \cot \theta_0}{\hat{R}} - \frac{\dot{\hat{R}}}{\hat{R}^2} (w + u \cot \theta_0) \right] \right\}, \end{aligned} \quad (\text{A3a})$$

$$\begin{aligned} \tau_{\varphi\varphi}^v = & \frac{2}{\hat{R}e_s} \frac{\dot{\hat{R}}}{\hat{R}} + \hat{\varepsilon} \left\{ \left(\frac{1}{\hat{R}e_s} + \frac{1}{\hat{R}e_{sh}} \right) \left[\frac{\dot{w} + \dot{u} \cot \theta_0}{\hat{R}} - \frac{\dot{\hat{R}}}{\hat{R}^2} (w + u \cot \theta_0) \right] \right. \\ & \left. + \left(\frac{1}{\hat{R}e_s} - \frac{1}{\hat{R}e_{sh}} \right) \left[\frac{\dot{w} + \dot{u}_\theta}{\hat{R}} - \frac{\dot{\hat{R}}}{\hat{R}^2} (w + u_\theta) \right] \right\}. \end{aligned} \quad (\text{A3b})$$

Finally, the contribution of the shear shell viscosity is incorporated to the tangential force balance [Eq. (A1)] which for a neo-Hookean shell assumes the form

$$\begin{aligned} \Delta F_{t,H}^1 = & \frac{k_B}{\hat{R}^4} (1 - \nu - \lambda_n)(w_\theta - \psi_\theta) + \dot{\psi}_\theta \left[\frac{\lambda_n}{\hat{R}^2} \left(\frac{1}{\hat{R}e_s} - \frac{1}{\hat{R}e_{sh}} \right) - \frac{2}{\hat{R}^2 \hat{R}e_{sh}} (1 - \lambda_n) \right] \\ & - \frac{2}{\hat{R}^3 \hat{R}e_{sh}} (\hat{R} \dot{w}_\theta - \dot{\hat{R}} w_\theta) - \dot{\psi}_\theta \left[\frac{\dot{\hat{R}} \lambda_n}{\hat{R}^3} \left(\frac{1}{\hat{R}e_s} - \frac{1}{\hat{R}e_{sh}} \right) - \frac{2 \dot{\hat{R}}}{\hat{R}^3 \hat{R}e_{sh}} (1 - \lambda_n) \right] \\ & - \frac{\chi}{2 \hat{R}^2 (1 - \nu^2)} \left[\dot{\psi}_\theta \frac{2 \hat{R}^2 (1 - \lambda_n) + \hat{R}^2 (1 - \nu) - (1 + \nu)}{\hat{R}} \right. \\ & \left. + w_\theta \frac{2 \hat{R}^2 + (1 + \nu) - \hat{R}^2 (1 - \nu)}{\hat{R}} \right], \end{aligned} \quad (\text{A4a})$$

and for a lipid-shelled microbubble reads

$$\begin{aligned} \Delta F_{t,MR}^1 = & \frac{k_B}{\hat{R}^4} (1 - \nu - \lambda_n)(w_\theta - \psi_\theta) + \dot{\psi}_\theta \left[\frac{\lambda_n}{\hat{R}^2} \left(\frac{1}{\hat{R}e_s} - \frac{1}{\hat{R}e_{sh}} \right) - \frac{2}{\hat{R}^2 \hat{R}e_{sh}} (1 - \lambda_n) \right] \\ & - \frac{2}{\hat{R}^3 \hat{R}e_{sh}} (\hat{R} \dot{w}_\theta - \dot{\hat{R}} w_\theta) - \dot{\psi}_\theta \left[\frac{\dot{\hat{R}} \lambda_n}{\hat{R}^3} \left(\frac{1}{\hat{R}e_s} - \frac{1}{\hat{R}e_{sh}} \right) - \frac{2 \dot{\hat{R}}}{\hat{R}^3 \hat{R}e_{sh}} (1 - \lambda_n) \right] \end{aligned}$$

$$\begin{aligned}
& - \frac{1}{3\hat{R}^8} \{w_\theta[6 - 6b + 4b\hat{R}^2 + 2b\hat{R}^8] + \psi_\theta[-2b\hat{R}^6 + 2\hat{R}^6 - 3\lambda_n + 2b\hat{R}^2 \\
& + b\hat{R}^6\lambda_n + 3b\lambda_n - 3b\hat{R}^2\lambda_n - b\hat{R}^8\lambda_n - \hat{R}^6\lambda_n]\}, \tag{A4b}
\end{aligned}$$

where $\lambda_n = n(n + 1)$.

-
- [1] K. Ferrara, R. Pollard, and M. Borden, Ultrasound microbubble contrast agents: Fundamentals and application to gene and drug delivery, *Ann. Rev. Biomed. Eng.* **9**, 415 (2007).
- [2] B. A. Kaufmann, K. Wei, and J. R. Lindner, Contrast echocardiography, *Curr. Probl. Cardiol.* **32**, 51 (2007).
- [3] K. Tsiglifis and N. Pelekasis, Nonlinear radial oscillations of encapsulated microbubbles subject to ultrasound: The effect of membrane constitutive law, *J. Acoust. Soc. Am.* **123**, 4059 (2008).
- [4] D. H. Thomas, P. Looney, R. Steel, N. Pelekasis, W. N. McDicken, T. Anderson, and V. Sboros, Acoustic detection of microbubble resonance, *Appl. Phys. Lett.* **94**, 243902 (2009).
- [5] A. Katiyar and K. Sarkar, Excitation threshold for subharmonic generation from contrast microbubbles, *J. Acoust. Soc. Am.* **130**, 3137 (2011).
- [6] N. de Jong, M. Emmer, C. T. Chin, A. Bouakaz, F. Mastik, D. Lohse, and M. Versluis, “Compression-only” behavior of phospholipid-coated contrast bubbles, *Ultrasound Med. Biol.* **33**, 653 (2007).
- [7] P. Marmottant, S. van der Meer, M. Emmer, M. Versluis, N. de Jong, S. Hilgenfeldt, and D. Lohse, A model for large amplitude oscillations of coated bubbles accounting for buckling and rupture, *J. Acoust. Soc. Am.* **118**, 3499 (2005).
- [8] K. Sarkar, W. T. Shi, D. Chatterjee, and F. Forsberg, Characterization of ultrasound contrast microbubbles using *in vitro* experiments and viscous and viscoelastic interface models for encapsulation, *J. Acoust. Soc. Am.* **118**, 539 (2005).
- [9] S. Paul, A. Katiyar, K. Sarkar, D. Chatterjee, W. T. Shi, and F. Forsberg, Material characterization of the encapsulation of an ultrasound contrast microbubble and its subharmonic response: Strain-softening interfacial elasticity model, *J. Acoust. Soc. Am.* **127**, 3846 (2010).
- [10] M. Overlede, Ultrasound contrast agents—Dynamics of coated microbubbles, Ph.D. thesis, University of Twente, Netherlands, 2009.
- [11] A. A. Doinikov, J. F. Haac, and P. A. Dayton, Modeling of nonlinear viscous stress in encapsulating shells of lipid coated contrast agent microbubbles, *Ultrasonics* **49**, 269 (2009).
- [12] M. A. Herrada, J. M. Montanero, and J. M. Vega, The effect of surface shear viscosity on the damping of oscillations in millimetric liquid bridges, *Phys. Fluids* **23**, 082102 (2011).
- [13] D. Barthes-Biesel and H. Sgaier, Role of membrane viscosity in the orientation and deformation of a spherical capsule in shear flow, *J. Fluid Mech* **160**, 119 (1985).
- [14] A. Lytra and N. Pelekasis, Static response and stability of coated microbubbles—Multiplicity of solutions and parameter estimation, *Fluid Dyn. Res.* **46**, 041422 (2014).
- [15] K. Tsiglifis and N. Pelekasis, Parametric stability and dynamic buckling of an encapsulated microbubble subject to acoustic disturbances, *Phys. Fluids* **23**, 012102 (2011).
- [16] M. Vlachomitrou and N. Pelekasis, Dynamic simulation of a coated microbubble in an unbounded flow: Response to a step change in pressure, *J. Fluid Mech.* **882**, 717 (2017).
- [17] C. C. Church, The effects of an elastic solid surface layer on the radial pulsations of gas bubbles, *J. Acoust. Soc. Am.* **97**, 1510 (1995).
- [18] D. B. Khismatullin and A. Nadim, Radial oscillations of encapsulated microbubbles in viscoelastic liquids, *Phys. Fluids* **14**, 3534 (2002).
- [19] P. Timoshenko and S. Woinowsky-Krieger, *Theory of Plates and Shells* (McGraw-Hill, Singapore, 1959).
- [20] C. Pozrikidis, Effect of membrane bending stiffness on the deformation of capsules in simple shear flow, *J. Fluid Mech.* **440**, 269 (2001).

- [21] D. Barthes-Biesel, A. Diaz, and E. Dhenin, Effect of constitutive laws for two-dimensional membranes on flow-induced capsule deformation, *J. Fluid Mech.* **460**, 211 (2002).
- [22] M. Vlachomitrou and N. Pelekasis, Numerical study of the interaction between a pulsating coated microbubble and a rigid wall. I. Translational motion, *Phys. Rev. Fluids* **6**, 013601 (2021).
- [23] M. Vlachomitrou and N. Pelekasis, Numerical study of the interaction between a pulsating coated microbubble and a rigid wall. II. Trapped pulsation, *Phys. Rev. Fluids* **6**, 013602 (2021).
- [24] S. Knoche and J. Kierfeld, Buckling of spherical capsules, *Phys. Rev. E* **84**, 046608 (2011).
- [25] A. Lytra, Numerical & theoretical study of the static response of coated microbubbles subject to uniform and distributed load: Application on the estimation of the shell elastic properties, Ph.D. thesis, University of Thessaly, 2017.
- [26] K. Tsiglifis and N. Pelekasis, Simulations of insonated contrast agents: Saturation and transient break-up, *Phys. Fluids* **25**, 032109 (2013).
- [27] K. Tsiveriotis and R. A. Brown, Boundary-conforming mapping applied to computations of highly deformed solidification interfaces, *Int. J. Numer. Methods Fluids* **14**, 981 (1992).
- [28] Y. Dimakopoulos and J. Tsamopoulos, A quasi-elliptic transformation for moving boundary problems with large anisotropic deformations, *J. Comp. Phys.* **192**, 494 (2003).
- [29] N. de Jong and L. Hoff, Ultrasound scattering of Albunex® microspheres, *Ultrasonics* **31**, 175 (1993).
- [30] L. Hoff, P. C. Sontum, and J. M. Hovem, Oscillations of polymeric microbubbles: Effect of the encapsulated shell, *J. Acoust. Soc. Am.* **107**, 2272 (2000).
- [31] S. M. van der Meer, B. Dollet, M. M. Voormolen, C. T. Chin, A. Bouakaz, N. de Jong, M. Versluis, and D. Lohse, Microbubble spectroscopy of ultrasound contrast agents, *J. Acoust. Soc. Am.* **121**, 648 (2007).
- [32] E. Lac and D. Barthes-Biesel, Deformation of a capsule in simple shear flow: Effect of membrane prestress, *Phys. Fluids* **17**, 072105 (2005).